Progress in Oceanography 237 (2025) 103529

Contents lists available at ScienceDirect

Progress in Oceanography

journal homepage: www.elsevier.com/locate/pocean

Evaluating the performance of an ensemble forecast system in predicting Loop Current Eddy separation in the Gulf of Mexico

Prasad G. Thoppil [a,*], Clark D. Rowley [a], Patrick J. Hogan [b], James Stear [c]

[a] Ocean Sciences Division, Naval Research Laboratory, Stennis Space Center, MS 39529, USA
[b] National Oceanic and Atmospheric Administration (NOAA), National Centers for Environmental Information (NCEI), Stennis Space Center, MS 39529, USA
[c] Chevron Technical Center Division, 1400 Smith Street, Houston, TX 77002, USA

ARTICLE INFO

Keywords:
Loop Current Eddy
Cyclonic eddies
Ensemble forecasting
Forecast uncertainty
Baroclinic instability
Frontal eddies
Deep ocean circulation

ABSTRACT

Forecasting mesoscale variability, such as the Loop Current (LC) growth and Loop Current Eddy (LCE) shedding in the Gulf of Mexico, poses challenges due to the large uncertainty in initial conditions and the development of non-linear instabilities from LC-cyclone interactions, which are crucial for LC/LCE separation. An ensemble forecast system may account for this uncertainty and filter out unconstrained scales and thereby extend the predictability of the mesoscale variability. A 32-member ensemble forecast system is employed to investigate the predictability of LC/LCE separation, with a specific focus on the December 2019 – March 2020 period. The forecasts demonstrated predictability of LC/LCE separation out to 7 to 13 weeks. During this period, significant changes occurred in the LC. The LC transitioned from being an extended LC to LCE separation on January 27, 2020. Subsequently, in March 2020, the LCE deformed and nearly split into two separate eddies. Detailed analyses of individual forecasts during this timeframe revealed that these transformations were influenced by two main interactions: (a) the interaction between the LC and a cyclone along its eastern edge, which caused the LC/LCE separation, and (b) the interaction between the LCE and a cyclone along its northern side, leading to the potential splitting of the LCE. These interactions were further intensified by the coupling between surface and deep cyclones. The validity of these findings is supported by a variety of observations, including drifters, current meters, and sea surface height, as well as verifying analysis.

1. Introduction

The Loop Current (LC) originates in the Caribbean and enters the Gulf of Mexico through the Yucatan Channel and exits through the Florida Straits as the Florida Current. At times, the LC extends far northwestward into the Gulf of Mexico, reaching speeds of 1.5–2 m s^{-1}, before turning clockwise toward the Florida Straits. As the LC extends, it forms a large, warm core, anticyclonic eddy by completing a clockwise circulation. This newly formed eddy, known as a Loop Current Eddy (LCE), typically has a horizontal scale of 200–400 km. The LCE may reattach to the LC and detach from it multiple times before eventually separating completely (Schmitz, 2005). This overall sequence is defined as LCE shedding. Following LCE shedding, the LC returns to a retracted position, while the detached LCE drifts westward into the Gulf. The LC and LCE dominate the upper circulation in the Gulf of Mexico (Oey, 2008; Sturges and Lugo-Fernandez, 2005) and serve as a major source of energy for deep eddies (Oey and Lee, 2002).

While extensive research has been conducted on the LC/LCE system (Hurlburt and Thompson, 1980; Vukovich and Maul, 1985; Hamilton et al., 2002; Zavala-Hidalgo et al., 2003; Schmitz, 2005), the mechanisms behind the LC/LCE separation and the role of deep eddies, particularly cyclones, in this process are not fully known (Pérez-Brunius et al., 2018; Furey et al., 2018; Zhu and Liang 2020). It is currently believed that the downstream growth of LC peripheral frontal eddies is significant for LCE formation (Cochrane, 1972; Fratantoni et al., 1998; Vukovich, 1988; Schmitz, 2005; Walker et al., 2009). These eddies on the eastern side of the LC, typically around 80–120 km in diameter and reaching depths of at least 1000 m, with surface geostrophic velocities of about 1 m s^{-1}, have been observed (Vukovich and Maul, 1985). These eddies often propagate westward and contribute to the detachment or separation of an LCE from the LC. The intensity of these perturbations tends to be more pronounced on the eastern side of the LC compared to

---

[*] Corresponding author.

E-mail addresses: prasad.g.thoppil.civ@us.navy.mil (P.G. Thoppil), clark.d.rowley.civ@us.navy.mil (C.D. Rowley), patrick.hogan@noaa.gov (P.J. Hogan), James.Stear@chevron.com (J. Stear).

https://doi.org/10.1016/j.pocean.2025.103529
Received 6 February 2025; Received in revised form 16 May 2025; Accepted 23 June 2025

the western side, indicating an amplification of cyclonic structures along the northern portion of the LC path (Vukovich, 1988). Schmitz (2005) emphasized the importance of having a pair of frontal eddies that help narrow the "neck" of the LC. This includes the presence of cyclonic eddies west of the LC along the Campeche Bank, as well as east of the LC along West Florida region. Cyclonic eddies formed along the northern edge of the LC also contribute to the shedding process in some cases. Oey (2008) found that deep cyclones, with depths exceeding 1500 m, are generated through the baroclinic instability of the LC. The study demonstrated that deep eddies tend to form along the LC path, particularly north of the Campeche Bank, with potential intensification along the West Florida Shelf. The findings concluded that deep cyclones at these locations represent the primary mode of variability at depth, which is phase-locked with the expansion of the LC and occasionally leads to shedding of an LCE. The modeling study of Le Hénaff et al. (2012) suggests that when upper layer frontal cyclones propagate over the Mississippi Fan, a deep cyclone is generated. Their simulation shows that this upper-deep cyclone pair moves across the LC and promotes the formation of LCE.

In previous studies investigating the dynamics of the LC and LCE, both non-data assimilative and data assimilative models have been used (Oey et al., 2003; Oey et al., 2005; Lin et al., 2007; Yin and Oey, 2007; Chassignet et al., 2007; Barth et al., 2008; Gopalakrishnan et al., 2013a, b; Xu et al., 2013; Hoteit et al., 2013; Huang et al., 2013; Rudnick et al., 2015; Rosburg et al., 2016; Morey et al., 2020). However, to the best of our knowledge, the study of LC/LCE shedding events in a real-time ensemble forecast system has not been previously explored. Here, we utilize the results from an ensemble forecast system for the Gulf of Mexico to demonstrate that the predictability of LC/LCE separation can be extended over deterministic (non-ensemble) systems, out to several weeks in some cases. The study focuses specifically on the LCE shedding event that occurred during the winter of 2019–2020 and the subsequent transformation of the LCE. Throughout this period, the dynamics of LC/LCE interactions with cyclones, particularly deep cyclones, are thoroughly examined.

The paper is organized as follows: Section 2 describes the ensemble forecast system and its configuration. Section 3.1 evaluates the overall forecast skill, followed by a comparison with satellite sea surface temperature (SST) observations in Section 3.2. Section 3.3 examines the evolution of LC and LCE in the verifying analysis (considered the truth) and validates these results using independent drifter velocity observations, which help identify key mesoscale features. Section 3.4 provides a detailed assessment of model predictability during the LC/LCE separation event around January 27, 2020. Section 3.5 investigates the structural evolution of the LCE after separation (by February 24), and its subsequent splitting into two eddies (by March 23). These sections also explore the processes driving LCE separation and transformation, with a particular focus on the role of deep cyclones, through the use of verifying analyses and individual forecasts, and validate the model's forecast performance using drifter data, along-track Sea Surface Height Anomaly (SSHA) observations, and the verifying analysis. Section 3.6 presents a comparison with other LCE separation events. Section 4 offers a broader discussion of the mechanisms responsible for deep cyclone formation and concludes with a summary of the main findings of the study.

2. Gulf of Mexico ensemble forecast system

In recent decades, significant progress has been made in global ocean prediction (Barton et al., 2020). Advances in this field involve various aspects, including increasing the horizontal and vertical resolution, fully coupled Earth System components (atmospheric-ocean-ice), as well as the development of ocean ensemble forecast systems (Jacobs et al., 2014; Jacobs et al., 2021, Sandery and Sakov, 2017; Barton et al., 2020; Thoppil et al., 2021). Additionally, advancements in data assimilation techniques including assimilation of velocity vectors and new Surface Water and Ocean Topography (SWOT) observations, and multi-scale approaches have proven effective in reducing forecast errors (Jacobs et al., 2014, Carrier et al., 2016; D'Addezio et al., 2019; Helber et al., 2023, 2022; Smith et al., 2023). While high-resolution models are capable of resolving mesoscale to sub-mesoscale features that closely resemble natural flow patterns, the generation of the unconstrained smaller scales can increase forecast errors and reduce overall skill.

The ensemble forecasting systems incorporate uncertainties in ocean initial conditions and are designed to extend forecast skill beyond that of single deterministic forecasts. The ensemble has been shown to improve forecast accuracy substantially – by nearly a factor of three compared to deterministic forecasts (Thoppil et al., 2021). This improvement is primarily due to non-linear filtering, which suppresses less-predictable, unconstrained scales in the model. Unlike any individual ensemble member, the ensemble mean benefits from averaging nonlinear solutions, which typically yields a lower Root Mean Square Error (RMSE) (Palmer, 2019a, 2019b). This nonlinear filtering effect is well documented in atmospheric modeling (Palmer, 1988; Surcel et al., 2014; Dobla-Reyes et al., 2005) and has been demonstrated in the ocean context by Thoppil et al. (2021). In their study, simulations initialized with the ensemble mean showed RMSE values comparable to the control forecast during the first 5–7 days. At longer lead times, however, growing dynamical instabilities degraded the skill of the control forecast, causing its error to converge with that of other deterministic members. In contrast, the ensemble mean maintained superior skill over time by effectively filtering out small-scale errors. Thus, ensemble forecast systems offer a robust means to reduce forecast uncertainty and increase predictive skill by leveraging the ensemble mean's ability to filter out unpredictable scales.

A 32-member ensemble forecast system for the Gulf of Mexico has been developed at the Naval Research Laboratory. This system combines the Navy Coastal Ocean Model (NCOM, Martin et al., 2009), the Navy Coupled Ocean Data Assimilation system (NCODA, Cummings, 2005) and the Coupled Ocean-Atmosphere Mesoscale Prediction System (COAMPS, Hodur, 1997). The domain covers the entire Gulf of Mexico with a 3 km horizontal resolution and 49 hybrid levels (33 sigma levels and 16 z-, or pressure levels). The vertical resolution is finest near the surface and gradually becomes coarser with depth. The Mellor-Yamada level 2 turbulent closure scheme is used for vertical mixing. The model incorporates tides as a lateral boundary condition, and monthly mean transports are used for riverine input. The model is initialized from an analysis produced by the NCODA system, thus allowing the assimilation of all available observations via a 24-hour incremental update cycle.

The NCODA system, which is the data assimilation component, utilizes a 3-D Variational technique (3DVar) for assimilating observations in near-real time. It incorporates a wide range of available observations, including satellite altimetry, sea surface temperature (SST), as well as profile observations from ships, gliders, and floats. The Modular Ocean Data Assimilation System (MODAS) ingests concurrent surface observations of temperature and sea surface height and is used to construct "synthetic profiles" that are projected downward through the water column and used to constrain the ocean interior (Fox et al., 2002). There is no assimilation of velocity observations in the system.

The ensemble system consists of two separate model runs. The first component is the control run, which represents a single deterministic forecast. The 24-hour forecast error variances from this control run are then used to generate perturbations to the model initial conditions through the Ensemble Transform (ET) methodology (Bishop and Toth, 1999; Wei et al., 2006). In addition, the initial condition perturbations generated by the forecast error variances are augmented by additional estimates of the model temporal variability, nowcast/analysis increments history, and climate variability so that the ensemble model perturbations will have a spread similar to the best guess of the control run analysis error variance. This is important, so that the distribution of ensemble solutions can encapsulate all detectable and dynamically relevant ocean states.

In addition to perturbing the initial conditions, the surface boundary conditions (COAMPS wind and heat fluxes, except solar radiation described in section 2.1) are also perturbed for the duration of the forecast using a space–time deformation technique with random shifting (Wei et al., 2013; 2016). This method addresses uncertainties in surface forcing by introducing random temporal shifts that simulate displacement and time lag errors in dominant dynamical features in the atmospheric forcing. For each ensemble member, the forcing is prepared at the same 3-hour interval, but the values are computed at randomly shifted times, using the linear interpolation of the original forcing fields. These time shifts are derived from independent random fields generated every 24 h with a specified spatial de-correlation scale, ensuring that interpolated fields are uncorrelated beyond a 24-hour interval. This approach results in independent atmospheric forcing for each ensemble member (Coelho et al., 2008; Wei et al., 2016). Detailed mathematical formulations are provided in Wei et al. (2013).

2.1. Surface and lateral boundary conditions

A short range (< 1 week) ocean forecast typically uses forecast output from an atmospheric prediction system to drive the surface momentum and heat fluxes, and a global ocean forecast system for lateral boundary conditions. The COAMPS has a forecast length of 5 days, so for extended range forecasts beyond 5 days, climatological forcing is constructed for the lateral and surface boundary conditions. For this purpose, 8 years of 3-hourly output (2005–2013) from the Central America COAMPS were used to generate an annual climatology of 3-hourly fields. This allows the climatological forcing to retain more synoptic character than monthly forcing. For each extended range forecast (91 days), the forecast from Central Americas COAMPS was used for the first 5-days of the forecast, and then smoothly transitioned to the climatological forcing for the remaining period. A similar method was used for the lateral boundary forcing. A daily climatology was constructed from 12-years (1994–2005) of output from a global HYCOM reanalysis (Metzger et al., 2014; Thoppil et al., 2016). For each extended range forecast, the first 5-days were from global HYCOM, and then transitioned to a daily climatology.

The ensemble forecast system provides a short range 24-hour forecast every day and a weekly 91-day long range forecast once a week. The results presented here cover the period from October 2019 to March 2020, focusing on the evolution, growth, LCE detachment and transformation following its separation from the LC. A series of forecasts initialized at various periods during this cycle were used to capture different stages of the LC/LCE interactions and subsequent evolution.

3. Results

3.1. Forecast skill and uncertainty

The extent of predictability of mesoscale variability in the Gulf of Mexico has been estimated using the model forecasts. We define the skill of the model as its ability to have lower root mean square error (RMSE) compared to the ground truth observations than a monthly mean

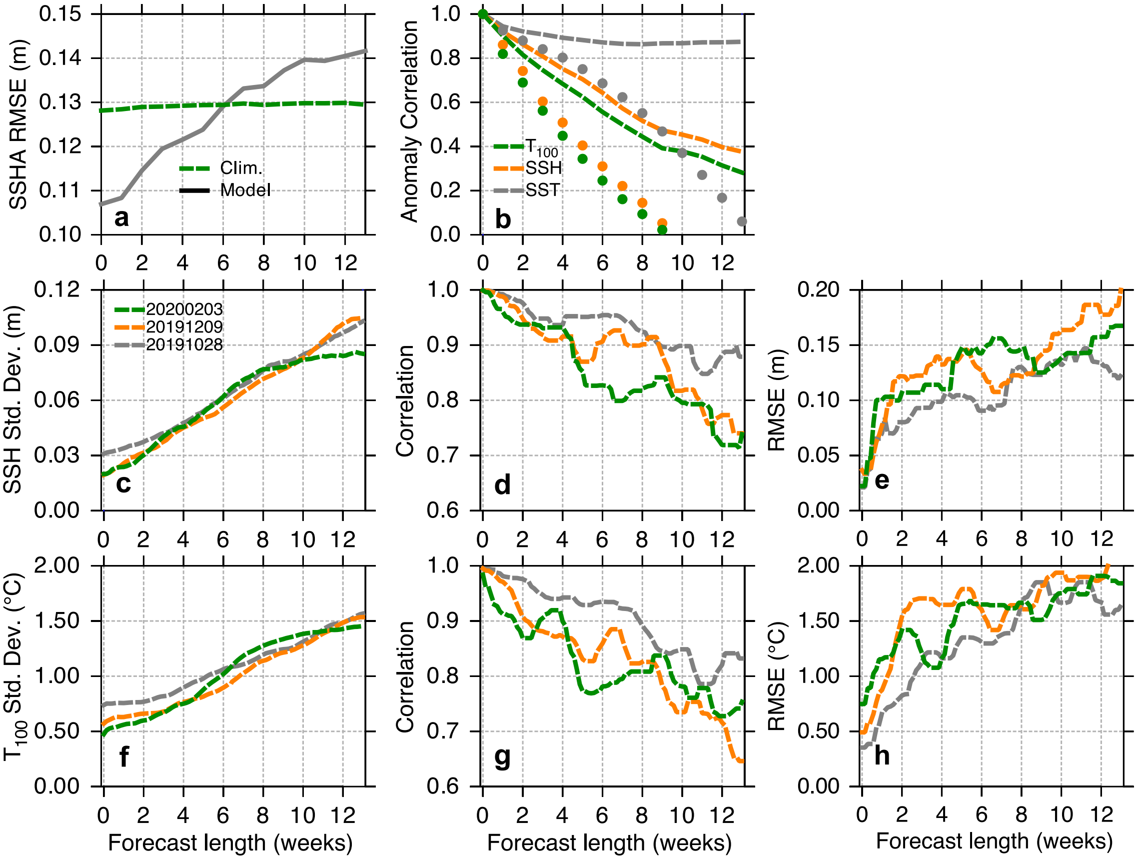

Fig. 1. Evaluation of ensemble forecast skill. (a) Root Mean Square Error (RMSE, m) of sea surface height anomaly (SSHA) from the ensemble mean (gray) and AVISO monthly climatology (green), computed against along-track altimetry observations for the Gulf of Mexico during 2020–2021. The AVISO climatology is based on the 1993–2018 period. Both model and AVISO are interpolated to altimeter tracks. (b) Anomaly correlation of ensemble-mean forecasts with the verifying analysis for sea surface height (SSH, orange) sea surface temperature (SST, grey), and temperature at 100 m (T_{100}, green), in the Loop Current region (90°–83°W, 22°–29°N) during 2019. Persistence skill is indicated by circles. Anomalies are calculated relative to the annual mean. (c) Ensemble spread (standard deviation) of SSH (m) versus forecast lead time. (d) Correlation coefficient and (e) RMSE of ensemble mean SSH, computed against the verifying analysis, from three 13-week forecasts initialized on October 28, 2019 (gray) December 9, 2019 (orange), and February 3, 2020 (green). (f–h) same as (c–e), but for T_{100} in the Loop Current region.

climatology of the ocean observations. The forecast error calculated using SSHA observations in the Gulf of Mexico exhibits superior skill out to 6 weeks (Fig. 1). The anomaly correlation in the LC region (90°–83°W, 22°–29°N) during 2019 reveals that the largest skill is for SST, with a skill exceeding 13 weeks. For SSH and temperature at 100 m (T_{100}), the skill extends up to 5–6 weeks. These variable specific skills reflect the availability of observations to constrain the features at the initial condition, with a higher number of SST observations resulting in the highest prediction skill. Compared to persistence, which assumes the model state remains unchanged by holding the analysis variables constant, the forecast outperforms persistence with a skill extending to 3 weeks for SSH and T_{100}, and 7 weeks for SST. The SST exhibits less variability compared to SSH and T_{100}, resulting in greater persistence and longer forecast skill.

To further quantify forecast error and associated uncertainty, we estimated correlation and RMSE between the ensemble mean forecast and the verifying analysis, as well as the ensemble spread (standard deviation across 32 ensemble members), from three 13-week forecasts initialized on October 28, December 9, 2019, and February 3, 2020, respectively (Fig. 1c–h). The ensemble spread, a measure of forecast uncertainty, for both SSH and T_{100} averaged in the LC/LCE region (90°–83°W, 22°–29°N) increases with lead times in all three forecasts (Fig. 1c, f). For the forecasts initialized on October 28 and December 9, the increasing spread reflects the uncertainty in capturing the transition from an extended LC state to LC/LCE separation. The 13-week and 7-week forecasts correspond to the LCE separation observed on January 27, 2020. Although the February 3 also shows increasing spread, it becomes less variant beyond approximately the 8-week lead time (green line). This suggests that after the LCE detaches on January 27, 2020, and undergoes transformation through March 23 (7-week lead), the system becomes more predictable as the LC retracts southward and the weakened LCE drifts westward. This post-separation phase is more predictable than the separation event itself, as indicated by the levelled off ensemble spread during the 8–13 week period.

The SSH (T_{100}) spread increases from 0.03 m (0.5 °C) to 0.1 m (1.5 °C) over the 13-week forecasts. The correlation coefficients decrease (Fig. 1d, g), and RMSE increases (Fig. 1e, h) with lead time. Among the three forecasts, the forecast initialized from October 28 maintains the highest correlation and lowest RMSE over the 13-week forecast horizon. Notably, around the 7-week lead time in the December 9 forecast, there is a peak in correlation (0.9) and a corresponding dip in RMSE for SSH, aligning with the timing of the LCE separation (orange line). Conversely, the February 3 forecast exhibits a modest RMSE increase between the 4- and 8-week lead times, attributed to mismatches in LCE transformation between the forecast and analysis (Fig. 1e). Overall, these metrics highlight the varying forecast skill across different stages of the LC/LCE evolution.

3.2. Formation and evolution of the Loop Current Eddy

High-resolution (1-km) satellite-derived sea surface temperature (SST, °C) observations on January 27 and March 23, 2020 illustrate the separation and transformation of the LCE, named eddy Thor (Fig. 2). On January 27, SST reveals the LCE near separation, indicated by the presence of relatively cold water along its southern edge. Concurrent drifter velocity observations (white vectors) align well with the LCE boundary and confirm that the LCE is separated by this date. The 7-week forecast initialized on December 9, 2019 and valid on January 27, 2020,

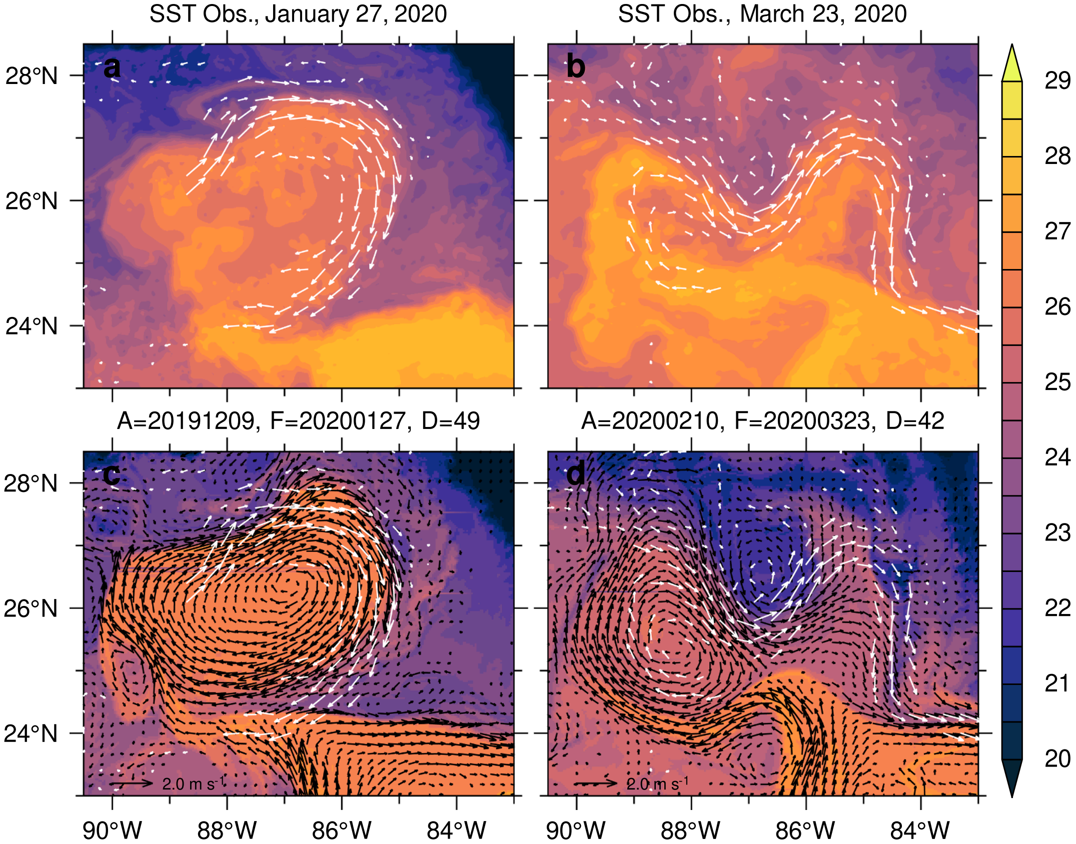

Fig. 2. Sea Surface Temperature (SST, °C) observations and model forecasts illustrating the evolution of the Loop Current Eddy (LCE). (a, b) SST observations on January 27 and March 23, 2020, respectively. (c) Model SST and surface currents (m s^{-1}) from a 7-week (49-day) forecast initialized on December 9, 2019 and valid on January 27, 2020. (d) Same as (c), but from a 6-week (42-day) forecast initialized on February 10, 2020 and valid on March 23, 2020. Forecasts are shown for ensemble member 1 (January 27) and ensemble member 26 (March 23), selected based on visual agreement with observations. White vectors represent drifter velocity observations from the 7 days preceding the valid time, binned onto a 0.4° × 0.4° grid. Vector magnitudes greater than 0.1 m s^{-1} are displayed.

successfully predicts the LCE separation (Fig. 2c), as indicated by both currents structure and SST pattern. However, the forecast places the LC-LCE separation farther north at ∼ 24.5°N, compared to ∼ 24°N in the drifter observations. Despite this spatial discrepancy, the forecast captures key features, including two frontal eddies visible in the satellite SST. A small cyclonic frontal eddy is represented along the western flank of the LCE (90°W, 25°N) in both forecast and observations, though with slight positional differences. A slightly larger frontal eddy along the northern edge of the LCE (~88°W, 27.5°N) creates a dip in the LCE in the SST observations. While the eddy itself is not clearly resolved in the forecast, a comparable dip is present, indicating consistent LCE deformation, likely driven by eddy-LCE interactions.

By March 23, 2020, the LCE undergoes substantial transformation, deforming into what appears to be two nearly separated eddies, as evidenced by both SST and drifter observations (Fig. 2b). The 6-week (42 days) forecast initialized on February 10, 2020 and valid on March 23 reasonably captures this LCE transformation (Fig. 2d), though some differences remain in the finer details. The forecast successfully captures a near-split LCE driven by the southward penetration of relatively cooler SST (between 86°W and 88°W), associated with a large cyclone along the LCE's northern boundary. This feature aligns well with drifter velocities and shows qualitative agreement with the SST observations. The ability of the model to represent both LCE separation and its deformation due to cyclonic frontal eddies suggests it can provide useful insights into the mechanisms triggering LCE separation.

3.3. Evolution of LC and LCE in the analysis

Here, we evaluate the analyses (truth) that served as initial conditions for the 13-week forecast, with a particular focus on constraining mesoscale features using observations. In Figs. 3 and 4, the weekly SSHA and surface currents from the analysis (truth) are compared to along-track altimeter SSHA and independent drifter observations from December 9, 2019 through March 23, 2020. This period encompasses the northwestward extension of the LC into the Gulf of Mexico, LC/LCE detachment, and the subsequent deformation of the LCE after separation. A qualitative agreement between the analyses and drifter observations indicates that mesoscale features, including the LC, LCE and cyclonic LC frontal eddies along the edge of the LC, are well-constrained during the data assimilation.

During December 9 – 16, 2019, the LC extended northwestward into the Gulf of Mexico, reaching north of 27°N (Fig. 3a, b). At this time, a weak cyclone on the eastern side of the LC started to emerge, indicated by SSHA low, although the cyclonic circulation is very weak. By December 23, a clear narrowing of the LC, referred to as necking down, is observed. Drifter observations on January 6 confirmed the presence of this cyclone, consistent with the SSHA patterns (Fig. 4e). The cyclone became progressively stronger and expanded westward, leading to the

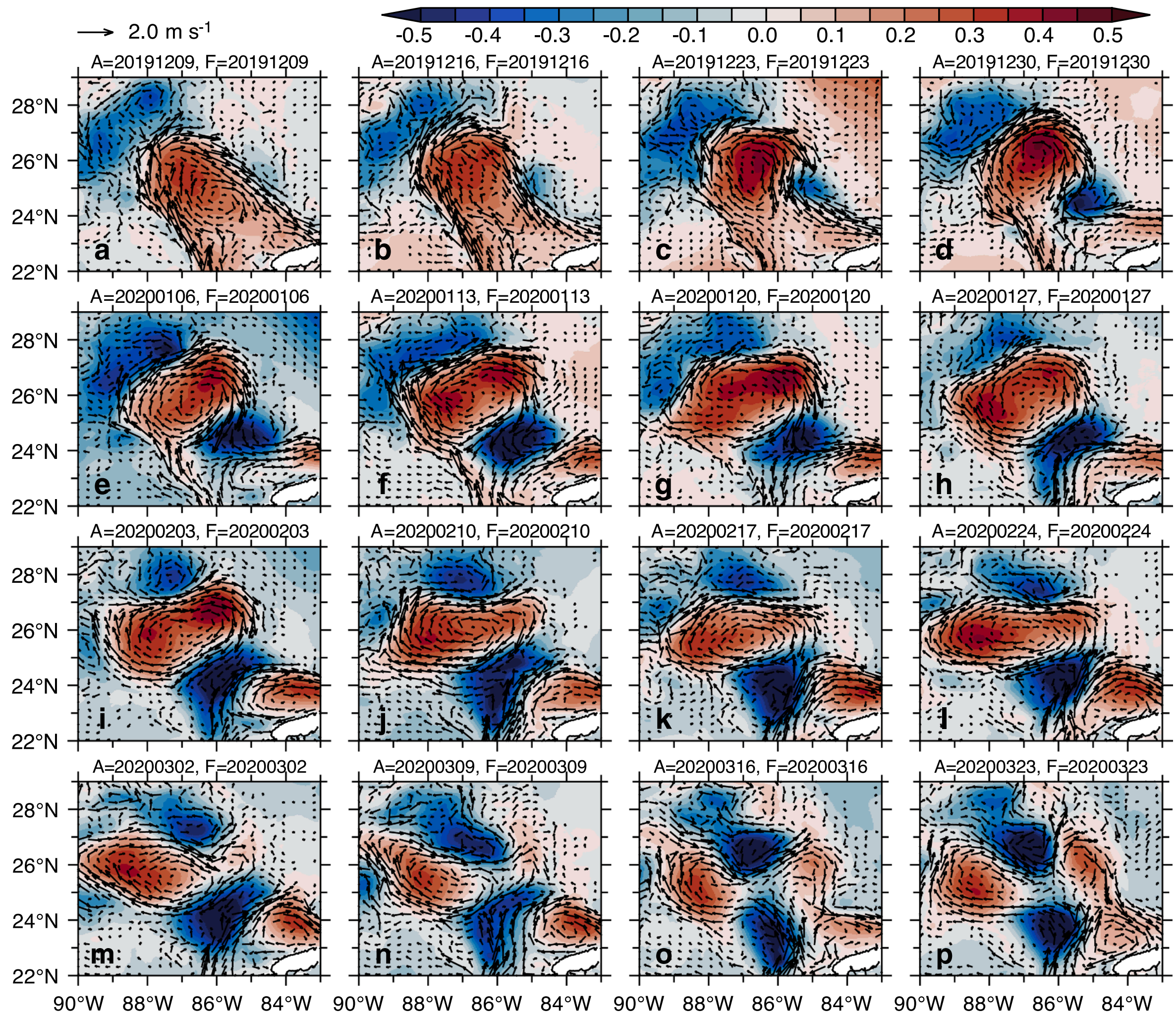

Fig. 3. Weekly ensemble-mean surface currents (m s^{-1}) and Sea Surface Height Anomaly (SSHA, m, shaded) from the analysis spanning December 9, 2019 to March 23, 2020. To facilitate comparison with along-track SSHA altimetry observations, a 20-year climatological mean SSH is subtracted from the model SSH to obtain SSHA (Thoppil et al. 2016). The vectors are shown for surface currents exceeding 0.1 m s^{-1}.

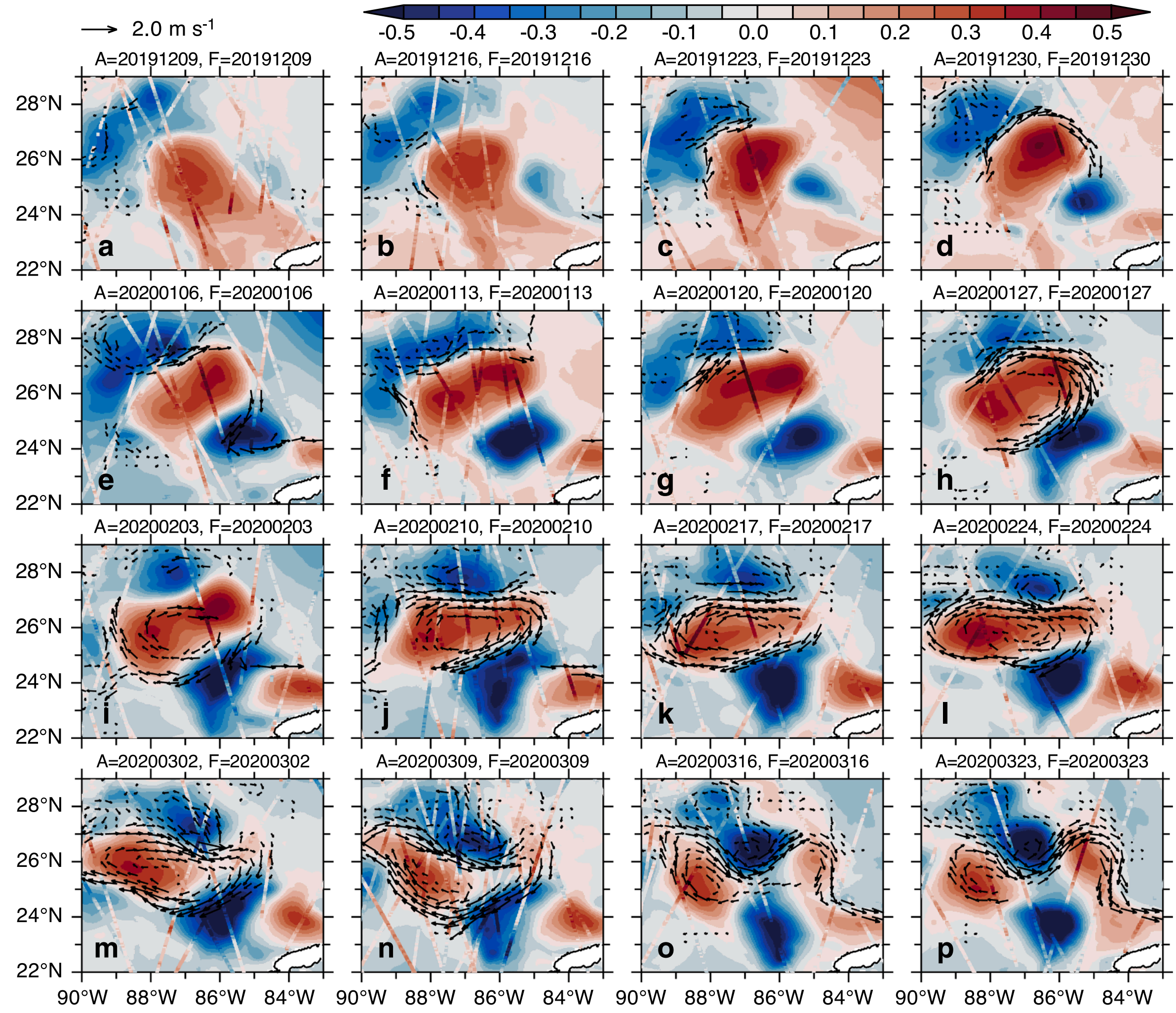

Fig. 4. Weekly currents at 50 m depth (m s^{-1}) derived from drifter observations, overlaid on ensemble mean Sea Surface Height Anomaly (SSHA, m, shaded) from the analysis spanning December 9, 2019 to March 23, 2020. For each panel, all available drifter observations from the 7 days preceding the analysis time are binned onto a 0.3° × 0.3° grid. Model SSHA is compared against along-track altimeter SSHA observations from the 5 days leading up to each corresponding analysis time.

detachment of the LCE from the LC by January 27, 2020 (Fig. 3h). The detachment of the LCE is determined based on a closed 0.17 m SSH contour and surface velocity fields, when sufficient drifter velocity observations are available. Drifter observations confirm the full detachment of the LCE, as drifters wrap around the closed loop to the south (Fig. 4h). In the remainder of the paper, the period around January 27 is referred to as the LC/LCE detachment period, based on this confirmation from the drifter data.

The separation of the LCE from the LC took approximately 4–5 weeks after the appearance of the cyclone on the eastern edge of the LC. Following the separation, the LC retracted to the south and formed part of the eastward flowing Florida Current. The persistent cyclone in the region prevented the LC from reattaching to the LCE. As the cyclone drifted west and southwest, following the LCE separation, the LC expanded and penetrated further north. Simultaneously, the LCE elongated zonally by ~ 450 km (between 85° and 89°W), with a slight clockwise rotation. By February 24, the LC had penetrated even farther north, reaching closer to the eastern flank of the LCE (Fig. 3l). There is good agreement between the drifter observations and the analyses, particularly regarding the location and size of the LCE (Fig. 4l).

The presence of a large cyclone to the north of LCE (86°W, 28°N), indicated by low SSHA, had significant impact on the subsequent evolution and transformation of the LCE. The location of this cyclone closely aligned with the drifter observations. Between February 3 and 24, the cyclone moved slightly eastward along the outer rim of the LCE. The south and southeastward penetration of this cyclone between March 2 and 23 led to a considerable weakening of the LCE through interaction with the LCE. By March 23, the cyclone had encroached further into the LCE, causing a partial split at the center while maintaining a connection in the south (Fig. 3p). The southward penetration of the cyclone in the model corresponds to the drifter observations (Fig. 4p). As the cyclone south of the LCE moved farther west (towards the Campeche Bank), the eastern part of the LCE reattached to the LC, which is also confirmed by the drifter and SST observations. The westward expansion of LCE is also limited by a cyclone during March 9 – 23 (located around 90°W, 25°N). Therefore, the frontal eddies associated with the LC have a strong influence on the evolution of both LC and LCE. The cyclone to the southeast of the LC triggers the LCE separation, while the cyclone to the north interacts with the LCE, causing significant weakening and a partial split.

It is worth mentioning that the sequence of events leading to eddy shedding and transformation is comparable to the case of the LCE Franklin in spring 2010 (e. g. Fig. 10 of Le Henaff et al., 2012). They also indicated the presence of a cyclone forming on the western side of the LC, along the northern slope of the Campeche Bank, which is not clearly evident in our analysis. In the following sections, the predictive skill of the LC and the LCE at various stages, potentially influenced by the large-scale features that are constrained during the analyses, will be assessed.

The model analyses demonstrate the ability of assimilated observations constrain mesoscale features consistent with independent drifter observations, particularly emphasizing the role played by the LC frontal eddies in the evolution of and transformation of the LC and the LCE. For brevity, the prediction skill will be evaluated out to 7 weeks unless noted otherwise.

3.4. LCE separation

3.4.1. Predictability and uncertainty of LCE separation

The predictability of the LCE separation event on January 27, 2020 is investigated using forecasts initialized from prior analyses up to 7 weeks in advance (Fig. 5). That is, the 7-week forecast initialized from December 9, 2019 analysis is valid on January 27, 2020 (Fig. 5h). In a perfect prediction system scenario, all forecasts should match the analysis (truth) on January 27, 2020 (Fig. 5a), and any departure from the truth represents the forecast error, which is expected to increase with longer forecast lead times. As shown in Fig. 5, the prediction system captures the LCE shedding event reasonably well at all lead times up to 7 weeks when compared against the verifying analysis, along-track altimetry SSHA, and drifter observations (Fig. 5). Specifically, the eastern flank of the LCE (around 85°W) agrees well with the drifter observations, and the presence of a cyclone on the eastern edge of the LC aligns with the altimetry observations. It should be noted that all drifter observations are confined to the eastern half of the LCE. Except during weeks 5–6 (Fig. 5f-g), when a cyclone along the northern edge of the LC pushed the LCE southward, the predicted LCE closely resembles that in the analysis and drifter observations. All forecasts exhibit either a clearly or nearly separated LCE triggered by the southeast cyclone. However, the location of this cyclone, while present in all forecast lead times, is confined slightly to the east compared to the analysis, where it expands across the entire LC. This mismatch can be used to explain the lack of a complete LCE separation in the forecast, especially at longer lead times (> 3 weeks). Although the model SSHA shows a distinctly separated LCE, part of the inflow through the Yucatan Channel remains connected to the LCE along the western portion of the LC in the > 3-week forecasts (Fig. 5d-h). In the analysis, this inflow is primarily confined to the east of 86°W, while its axis is slightly shifted to the west in the forecasts. Consequently, a retracted LC is not evident in the forecast at longer lead times. Despite these discrepancies, the forecasts demonstrate great accuracy in predicting the timing of the LCE separation.

The presence of a large cyclone to the north and northwest of the LCE in the analysis, indicated by low SSHA and drifter observations, influences northward expansion of the LCE (Fig. 5a). Due to a slightly different location of this cyclone in the forecasts (Fig. 5b-h) compared to the analysis (Fig. 5a), the structure, shape, and northward expansion of the LCE differ in the forecasts. In particular, the south and southeastward expansion of the cyclone relative to the analysis and its interaction with the LCE result in a slightly deformed LCE in the weeks 5–6 forecasts (Fig. 5f-g). Although the characteristics of the cyclone located northwest of the LC in the analyses (as indicated by negative SSHA) during December 9 – 30, 2019 (Fig. 3a-d) are not significantly different, the structure of the LCE is better depicted in the 7-week forecast (initialized from December 9 analysis) compared to the 5–6 weeks forecast (Fig. 5). This suggests that even a slight perturbation arising from the non-linear interaction between the LCE frontal eddies and the LCE can lead to large forecast errors that are difficult to accurately predict. It is important to note that the deformed LCE in the weeks 5–6 forecast is not an unrealistic behavior of the model, rather, the interaction occurs early in the forecast, particularly in the forecasts initialized from the December 16 and 23 analyses (Fig. 3b-c).

In the ensemble forecast system, the ensemble mean is considered the best estimator, while the ensemble spread serves as a measure of uncertainty associated with the prediction (Counillon and Bertino, 2009). Ensemble averaging filters out unconstrained scales and improves overall skill compared to a deterministic forecast (Thoppil et al. 2021). To evaluate the accuracy of the ensemble forecast, Fig. 6 shows the spaghetti plot of the 0.17 m SSH contours for each ensemble member, which helps identify the position of the LC and LCE (Leben, 2005; Dukhovskoy et al., 2015), as well as the transition region indicative of LCE formation. As expected, the ensemble spread (calculated as the standard deviation across the 32 ensemble members) increases with the forecast lead times as indicated by the shaded regions. The small ensemble spread at the analysis (Fig. 6a), indicated by closely packed 0.17 m SSH contours, is a result of the mesoscale features being constrained by the data assimilation process. As dynamical instabilities

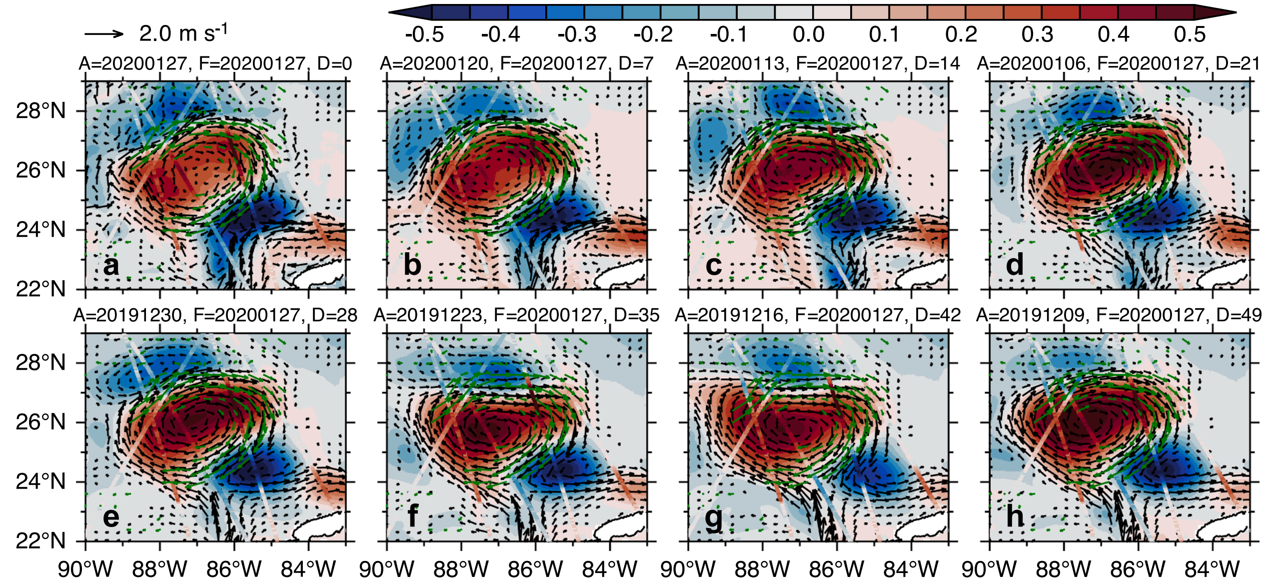

Fig. 5. Ensemble mean surface currents (m s^{-1}) and Sea Surface Height Anomaly (SSHA, m) from forecasts initialized up to 7 weeks prior and valid on January 27, 2020. Surface current panels are overlaid with drifter velocity observations (green vectors) and along-track SSHA altimetry observations during the 7–day and 5–day periods preceding the valid time, respectively. Drifter observations are binned onto a 0.4° × 0.4° grid. The first panel represents the verifying analysis, which serve as the reference against which all prior forecasts are compared. Vectors are displayed for currents exceeding 0.1 m s^{-1}. The forecast initialized from the December 9, 2019 analysis (A = 20191209) is valid on January 27, 2020 (F = 20200127) corresponding to a 7-week lead time (D = 49 days).

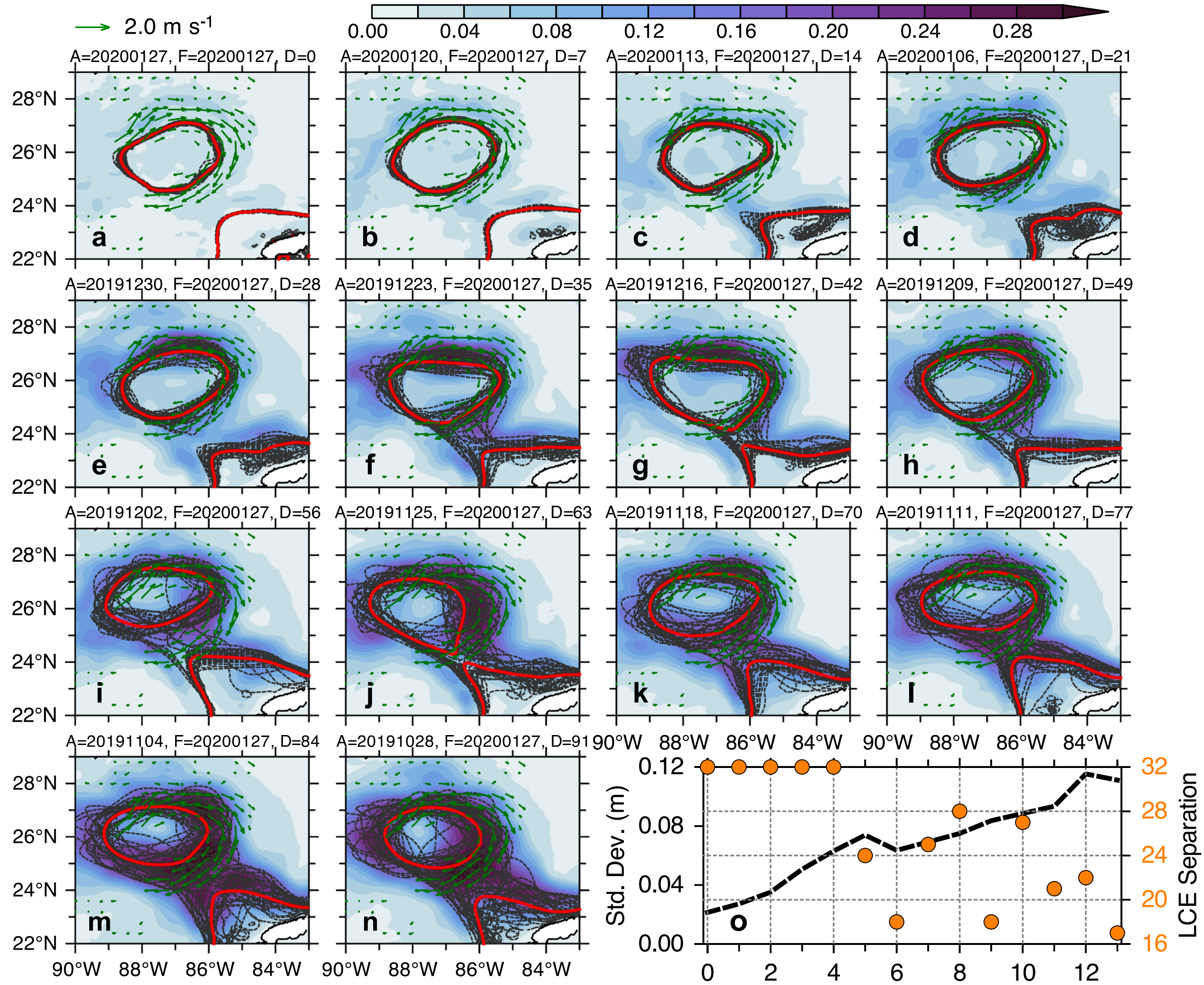

Fig. 6. Ensemble standard deviation (spread) of the sea surface height (SSH, m; shaded) from forecasts initialized up to 13 weeks prior and valid on January 27, 2020. Drifter velocity observations (green vectors) during the 7–day period preceding the valid time are superimposed and binned onto a 0.4° × 0.4° grid. The 0.17 m SSH contours, indicating the location of the Loop Current/Loop Current Eddy (LC/LCE), are overlaid for all 32 ensemble members (dashed lines) and the ensemble mean (red line). Panel (o) depicts the region averaged ensemble SSH spread (dashed line; 90°–83°W, 22°–29°N) and the number of ensemble members predicting the LC separation (orange circles) as a function of forecast lead time in weeks (x-axis).

grow in the forecast, the forecast skill decreases, leading to a larger spread, especially in the region surrounding the energetic LCE. Although the ensemble spread generally increases with lead time, the spread from the 6- and 13-week forecasts is slightly smaller than that from the previous forecasts (Fig. 6o). Since each forecast is initialized from a different analysis constrained by the availability of observations at the time, variations in the resulting spread across forecasts are expected. Additionally, the ensemble spread is influenced by the evolving state of LC/LCE system – certain stages of evolution may be more predictable than others. For instance, the timing and location of LC/LCE separation is generally less predictable than the subsequent evolution of a detached LCE.

The ensemble mean at all forecast lead times consistently shows a closed 0.17-m SSH contour, indicating a detached LCE with a retracted LC. However, the number of ensemble members predicting LCE separation varies across lead times, with more than 50 % showing separation (Fig. 6o). In the weeks 1–4 forecasts (Fig. 6b-e, o), all ensemble members predict a clearly detached LCE. By weeks 5–13 forecasts (Fig. 6f-h), a bimodal pattern emerges: some members show an attached LC/LCE, while others depict a separated LCE. In members still exhibiting attachment, the LC appears constricted at the separation location. The number of ensemble members predicting separation in the 5-, 6-, and 7-week forecasts are 24, 18 and 25, respectively. At week 8, 28 members predict separation, but this drops to 18 at week 9, reflecting forecast sensitivity to the initial analysis. This difference is evident in the ensemble mean: the 0.17 m contour in the 9-week forecast is nearly attached to the LC, whereas it is clearly detached at week 8. In the 13-week forecast, 17 members predict LCE separation (Fig. 6n). While both modes are dynamically plausible, the ensemble spread highlights areas of forecast uncertainty, providing valuable insights for decision making. Overall, the ensemble mean (red line) agrees relatively well with the drifter observations, indicating the skill of the ensemble forecast system in capturing the behavior of the LC and LCE.

3.4.2. *Evolution of upper and deep ocean circulation*

A 7-week forecast initialized from the December 9, 2019 analysis is used to investigate the deep cyclone and its role in the evolution of the LC and subsequent LCE separation (Fig. 7). The choice of this forecast is based on the fact that the cyclone responsible for triggering the LCE separation was not a constrained feature during the analysis, yet the forecast is able to reasonably reproduce the separation event. During the analysis, the LC extends northwestward into the Gulf of Mexico, reaching north of 27°N (Fig. 7a). Northwest of the LC, a weak cyclonic circulation, as indicated by low SSHA, dominates the circulation. At the

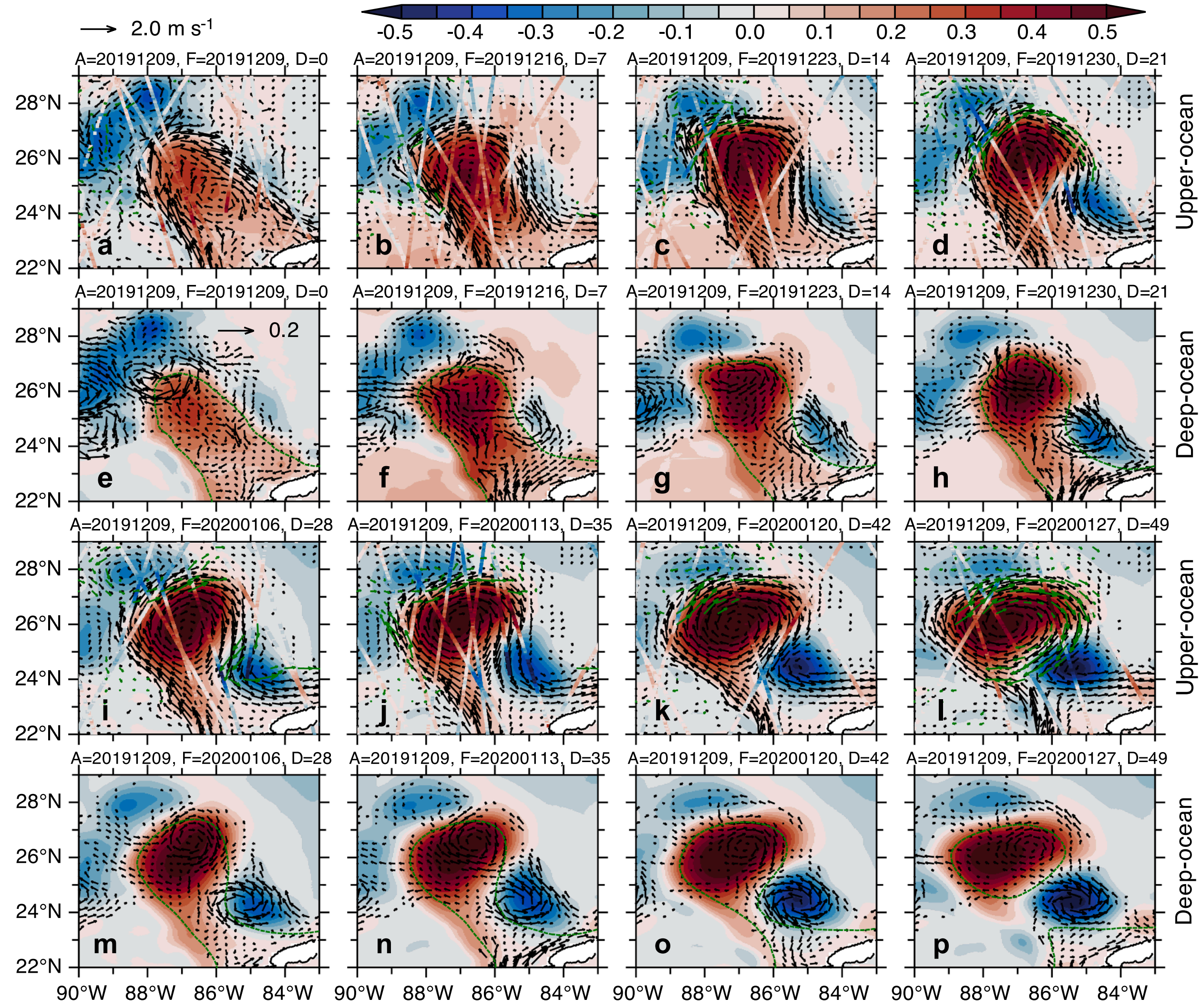

Fig. 7. Ensemble mean surface currents and deep currents (averaged over 1000–2000 m) (m s^{-1}), and Sea Surface Height Anomaly (SSHA, m) from a 7-week forecast initialized from the December 9, 2019 analysis. Surface current panels are overlaid with drifter velocity observations (green vectors) and along-track SSHA altimetry observations during the 7–day and 5–day periods preceding each forecast lead time, respectively. Drifter observations are binned onto a 0.4° × 0.4° grid. Deep current panels include the 0.17 m Sea Surface Height (SSH, m) contour. Vectors are displayed for surface (deep) currents exceeding 0.1 (0.02) m s^{-1}. The reference vector for surface (deep) current is 2 (0.2) m s^{-1}.

deep levels, a small anticyclone is evident on the northern tip of the LC at 87°W, 26°N (Fig. 7e). However, neither the surface nor deep circulation during the analysis show a cyclone, despite the presence of a weak SSHA low east of the LC. This further reinforces the claims that the predictability of the LCE separation does not rely on the cyclone present in the analysis, providing confidence in the results.

A week later (December 16, Fig. 7b), the surface circulation remains similar to the analysis, with a slightly stronger LC. However, a deep cyclone starts to develop at 85°W, 24.5°N (Fig. 7f). As the deep cyclone strengthens, its signature becomes clearer in the surface circulation. That is, the development of the deep cyclone slightly precedes the surface cyclone. The surface signature of the cyclone becomes apparent only around December 30 when it induces the development of a neck along the eastern side of the LC. As the deep cyclone continues to strengthen, it cleaves the LC, leading to the development of necking (e.g. Schmitz, 2005; Oey, 2008), which triggers the separation of the LCE on January 27, 2020 (Fig. 7l, p).

The comparison between the forecast and the along-track SSHA and drifter observations reveals several qualitative agreements in the sequences of events leading to the formation of the LCE. The northeastern outer edge of the LC at the 3-week forecast (December 30; Fig. 7d) aligns well with the drifter observations. The northern extent of LC is closely aligned with the along-track SSHA, although there are some differences in the exact location of the LC edge. However, in other areas, there are some discrepancies between the forecast and the along-track SSHA. The westward expansion of the cyclone at week 3 is underpredicted compared to the along-track SSHA observations (Fig. 7d). Additionally, despite intensification, the cyclone in the forecast exhibits minimal westward movement, contrary to what is observed in the analysis (Fig. 3a-h). These differences in the position and strength of the cyclone can contribute to discrepancies in the exact timing of LCE formation between the forecasts and the analysis (Figs. 7 and 3). Apart from the cyclone induced changes, the forecast shows minimal transformation of the LC in January 2020, which is consistent with the verifying analysis and observations.

The deep circulation features in the forecasts (Fig. 7f, h, n, p) are compared to the verifying analysis (Fig. 8a-d). The evolution of the deep cyclone in the forecasts, particularly its location (85°W, 24.5°N), and the presence of a well-developed deep cyclone in the forecasts from weeks 2 to 4, is similar to the analysis, albeit the details differ. Consistent with the analysis, the deep cyclone in the forecasts does not show significant westward propagation, and it is slightly stronger than the analysis.

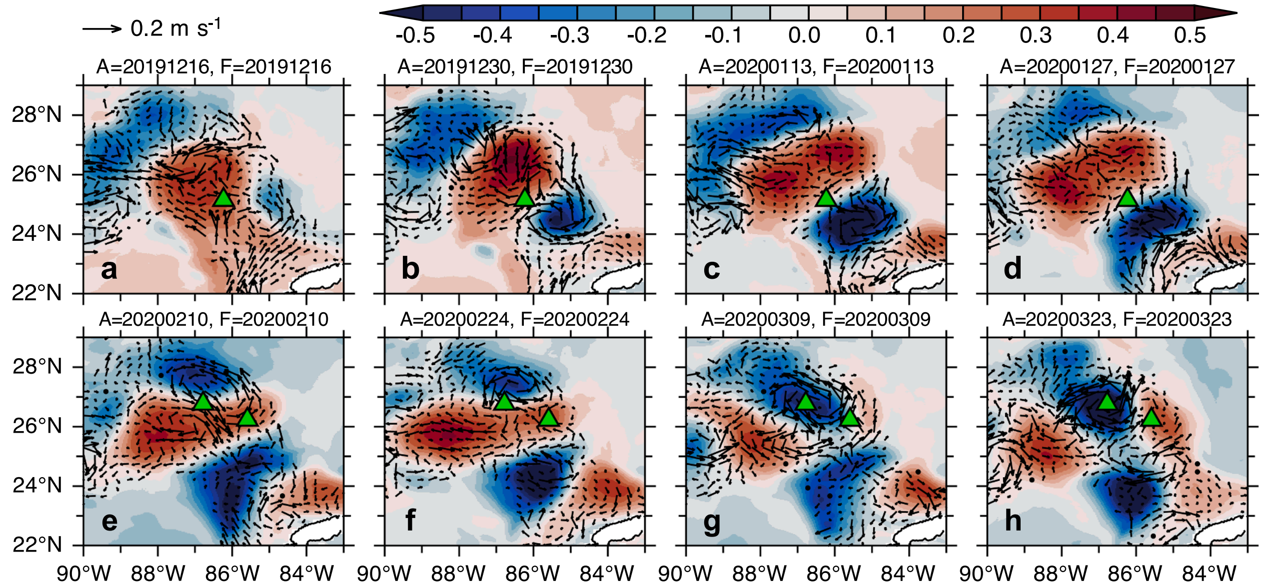

Fig. 8. Bi-weekly ensemble-mean deep currents (m s^{-1}), averaged over 1000 – 2000 m depth, from the analysis spanning December 16, 2019 to March 23, 2020. Ensemble mean Sea Surface Height Anomaly (SSHA, m) is overlaid to illustrate the relationship between deep cyclones and the surface circulation. The locations of the current meter observations E05 (top panels; see Fig. 10), and B04 and C06 (bottom panels; see Fig. 18), are marked by filled triangles. Vectors are shown deep currents exceeding 0.02 m s^{-1}.

Additionally, the forecasts successfully depict a deep anticyclone beneath the LC, although it appears to be more organized in the forecast compared to the analysis. It is worth noting that Donahue et al. (2016) have also reported the presence of one or more deep mesoscale features before the detachment of the LCE.

The comparison of the vertical structure of zonal velocity within the

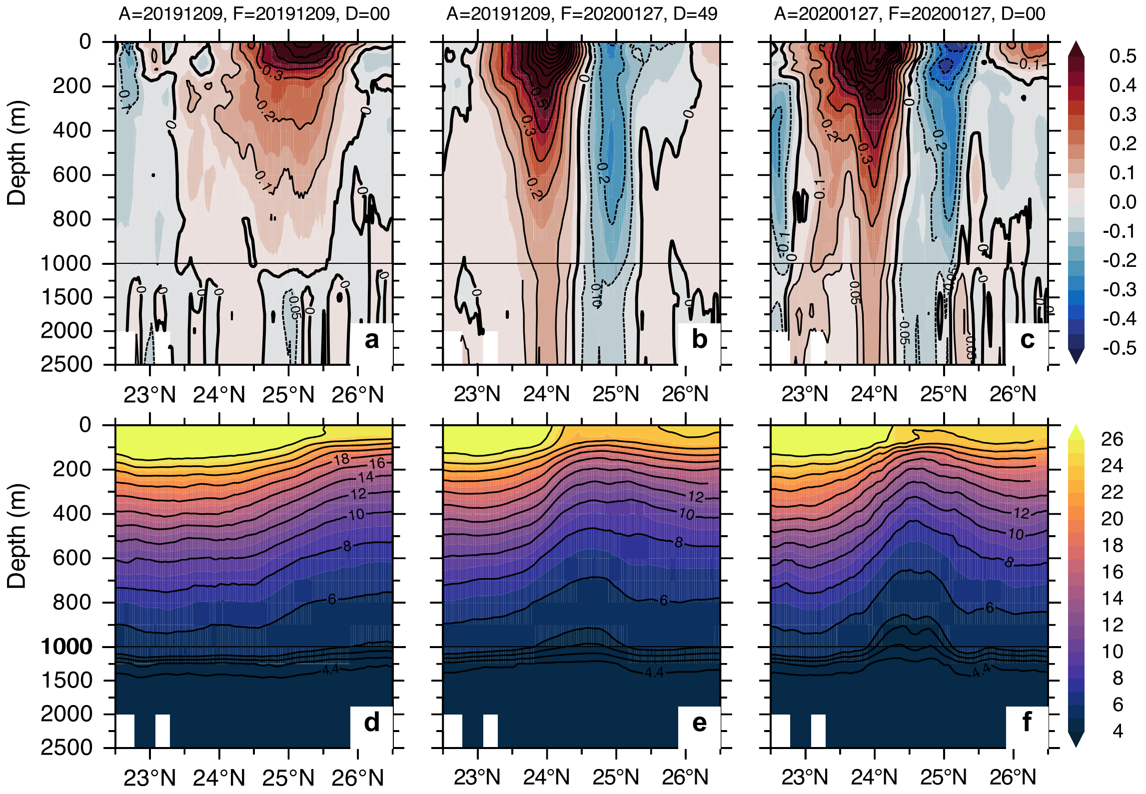

Fig. 9. Vertical sections of (a-c) zonal velocity (m s^{-1}) and (d-f) temperature (°C), comparing (a, d) the analysis on December 9, 2019; (b, e) the 7-week forecast initialized on December 9, 2019 and valid on January 27; and (c, f) the verifying analysis on January 27, 2020. All fields are averaged over the region 84.5°–85.5°W. Positive (negative) velocity indicates eastward (westward) flow. The westward current around 25°N indicates the northern flank of the cyclone. Contour intervals are 0.1 m s^{-1} for velocity and 2 °C for temperature (note that contour intervals differ below 1000 m). The 7-week forecast fields use the average of the first three ensemble members to better capture the core of the current associated with the cyclone, while the 32-member ensemble mean reveals a similar structure with reduced intensity.

cyclone between the 7 weeks forecast (Fig. 9b) and the verifying analysis (Fig. 9c) reveals good qualitative agreement, further highlighting the model's skill in representing the cyclone. The southern flank of the cyclone, characterized by eastward flow with a core at 24°N, and the westward flow in the north qualitatively compare with the analysis. A surface intensified eastward flow with velocities exceeding 1 m s^{-1} is evident, demarcating the corresponding westward flow at 24.5°N. That eastward flow gradually decreases to 0.5 m s^{-1} at 250 m. The westward flow on the northern part of the cyclone, centered at 25°N, reaches a peak velocity of 0.2 m s^{-1} in the forecast, slightly weaker than the analysis value of 0.25 m s^{-1}. Both the model and the analysis indicate a deep cyclone with velocities ranging from 0.05 to 0.1 m s^{-1}.

The temperature vertical section across the cyclone in the 7-week forecast (Fig. 9e) compares reasonably well with the analysis (Fig. 9f)). The forecast shows similar shoaling of the isotherms, although the difference is more pronounced at deeper isotherms where the analysis exhibits a sharper vertical displacement of the isotherms. For example, the 5 °C isotherm at 24°N shoaled by 100 m from 1000 m to 900 m in the forecast, compared to 150 m in the analysis. However, the location of the 5 °C isotherm is comparable between the analysis and the forecast. Based on the location of the 5 °C isotherm at 1000 m, the approximate diameter of the deep cyclone can be estimated to be 120 km (24° – 25.1°N). The analysis suggests that the deep cyclone has a signature that extends below 1000 m depth. The characteristics of the deep cyclone in the model are in good agreement with the observations by Vokovich and Maul (1985) and model simulation results by Le Hénaff et al. (2012), particularly regarding the location of the 5 °C isotherm and its vertical displacement.

The analysis on December 9, 2019 (Fig. 9a, d), which served as the initial condition for the 7-week forecast, does not indicate the presence of a surface or deep cyclone. This confirms that the development of the cyclone in the forecast is not constrained by the analysis. The flow in the upper 1000 m is eastward, representing the eastern flank of the LC with its core located around 25°N. However, there is a weak westward current of 5 cm s^{-1} below 1000 m, suggesting favorable conditions for the development of a deep cyclone. The deep thermocline associated with the LC, as indicated by the 26 °C isotherm south of 25.5°N, gradually shoals north of 24.5°N, with a more pronounced shoaling observed at deeper isotherms. In the 7-week forecast, the retreat of the 26 °C isotherm to the south of 24°N is accompanied by the development of a cyclone.

3.4.3. *Deep cyclone validation*

Independent deep current meter observations (Johnson et al., 2022) are used to validate the existence of a deep cyclone during the period of LCE separation (December 2019 – January 2020). The time-series of velocity vectors at 86.23°W, 25.15°N, displayed in Fig. 10, demonstrate the highly variable nature of the deep currents. Note that the current meter was located at the northwestern boundary of the deep cyclone (see current meter location in Fig. 8). During December 1–23, 2019, the flow was predominantly southwesterly to strong westerly. As the deep cyclone expanded into the current meter location, the flow shifted to predominantly southward, likely capturing the western flank of the cyclone. This southerly flow persisted until January 20, when it gradually became northwesterly. The model analysis currents (red vectors) exhibit a similar pattern, confirming that the timing of the southward flow coincides with the presence of the deep cyclone. Furthermore, the magnitude of flow (10–20 cm s^{-1}) aligns well with the model analysis, indicating consistence between the observations and the model representation of the deep currents. There is, however, a notable directional difference between December 17 and 25, where the model current is predominantly southwesterly, in contrast to the persistent westward flow observed.

3.4.4. *Predictability of deep cyclone*

It is evident from the preceding discussion that the development of a deep cyclone around December 16, 2019 (Fig. 7b) played a crucial role in the separation of LCE in January 27, 2020. The representation of this cyclone on December 16, at different leading times going back 7 weeks, could provide further insights into its generation (Fig. 11). All forecasts consistently predicted the presence of a deep cyclone in the West Florida shelf region, including the 7-week forecast initialized from the October 28, 2019 analysis (Fig. 11h). Although the shape of the cyclones in these forecasts ranges from partially to fully closed compared to the analysis (Fig. 11a), there is general agreement on their location around 85°W, 24.5°N. The formation of the deep cyclone is accompanied by stronger northward inflow through the Yucatan Channel into the Gulf of Mexico, which is believed to contribute to its generation. The analysis reveals that this inflow through the Yucatan Channel then turns northeast to form the eastern flank of the deep cyclone. All forecasts consistently captured this flow pattern, although some variations in the flow are evident among the different forecast lead times. Additionally, the forecasts also show a deep anticyclone located predominantly north of 26°N, although its strength varies at different lead times and is comparable to that in the analysis. The influence of this anticyclone on the position of the deep cyclone remains uncertain. Further investigation is needed to determine the extent to which the anticyclone impacts the location and behavior of the deep cyclone.

If the formation and progressive strengthening of the upper and deep cyclone play a dominant role in the separation of the LCE, it is plausible to expect that a 13-week forecast initialized on October 28, 2019, could potentially predict the LC/LCE separation event that occurred on January 27, 2020. As expected, the 13-week forecasts initialized from October 28 analysis, as shown in Fig. 12, are able to predict the LCE separation realistically on January 27. The sequence of events leading to the separation is consistent with the observations. The analysis during October 28, 2019 (Fig. 12a) show a retracted LC confined to the south of 25°N, with a large region of weak cyclonic circulation (negative SSHA) to the north. The LC becomes stronger and extends farther northwestward into the Gulf of Mexico, reaching 27°N by week 6 (Fig. 12d). At weeks 8, (Fig. 12i) a constricted, or "necking" LC with a cyclonic signature located to the southeast of the LC, indicated by low SSHA, is

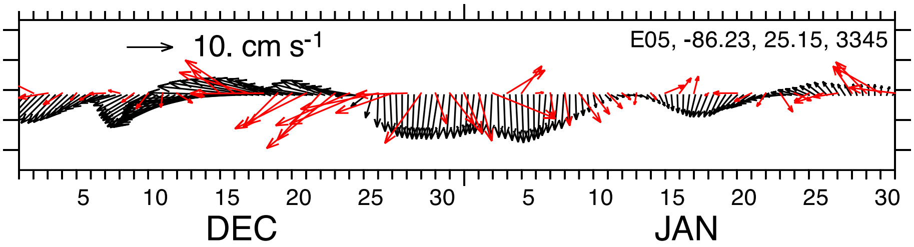

Fig. 10. Time-series of vector velocity at E05 (86.23°W, 25.15°N), 3345 m depth from (black) current meter observations and (red) model current from the analysis, but at 1500 m depth (owing to the last depth being saved during the analysis). The period December 2019 – January 2020 covers the presence of deep cyclone along the eastern edge of the LC. The current meter was located at the northwestern edge of the deep cyclone as indicated by the triangle in Fig. 8. Hourly velocity observations are smoothed using a 49-hour Parzen filter.

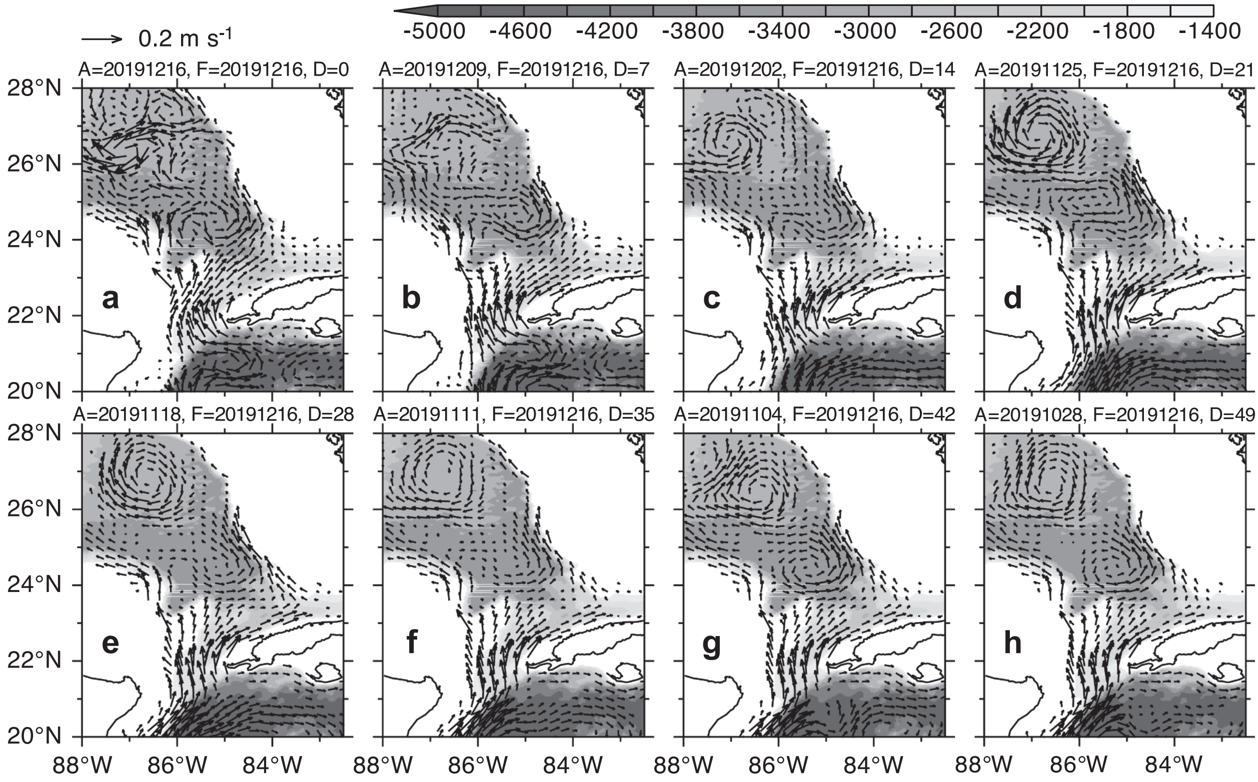

Fig. 11. Model subsurface currents (m s^{-1}) at 1500 m on December 16, 2019, from forecasts initialized up to 7 weeks prior. The analysis on December 16, 2019 (Day = 0) serves as the reference truth for evaluating the accuracy of earlier forecasts. Shading indicates model bathymetry (m). Vectors are shown for current magnitudes exceeding 0.02 m s^{-1}.

evident. That cyclone continued to intensify, eventually triggering the separation of the LCE on January 27, 2020. Although the location of LCE aligns well with the drifter observations at week 13 (91-day), the LC and LCE in the forecasts remains connected along the western side of the LC. In fact, a fully separated LCE from the LC occurred the week before, on January 20 (Fig. 12k). As expected, there are obvious difference in forecast skill or spread between the 13-week and 7-week forecasts as indicated by the spread of a 0.17 m SSH in Fig. 6. The 13-week forecast has larger uncertainty in predicting a detached LCE with the number of ensemble members predicting a detached LCE is 17 compared to 26 in the 7-week forecast.

By comparing the 7-week (Fig. 7l, p) and the 13-week (Fig. 12l, p) forecasts, both valid on January 27, but initialized at different times (December 9 versus October 28, respectively) we can gain further insights into the influence of the initial condition on the predictability of LCE separation. As expected, there are differences in the characterization of the LC at the initial conditions (analysis) in these forecasts, more so in the deep ocean than the surface. The analysis on October 28 (Fig. 12a, e) represents the early stages of LC development and does not exhibit clear signatures of surface and deep cyclones on the eastern side of the LC. It is not until the 6-week forecast (December 9; Fig. 12h), that a deep cyclone begins to appear, although its signature is weak. The deep cyclone gradually intensifies until 10-week forecast on January 06 (Fig. 12n), followed by a weakening in the subsequent weeks. Although the location of the deep cyclone is consistent among the forecasts, it is somewhat weaker in the 12- and 13-week forecasts (Fig. 12o, p). Thus, both forecasts initialized from December 9 (Fig. 7a, e) and October 28 (Fig. 12a, e) share a common feature: the evolution of a deep cyclone. This cyclone's development, irrespective of the initial conditions, played a crucial role in enhancing the predictability of the LCE separation.

The December 9 analysis (Fig. 7a, e) does show a small region of negative SSHA along the northeastern LC, although no distinct surface or deep cyclonic circulation is evident. However, by comparing with the 13-week forecasts initialized from the October 28 analysis, it can be argued that the presence of the small region of negative SSHA at the analysis during December 9 had no significant impact on the predictability of the LCE. Instead, the forecast system consistently simulated the deep cyclone (Fig. 11), regardless of the initial conditions, which played a crucial role in enhancing the predictability of the LCE separation.

The vertical section of temperature and zonal velocity across the cyclone exhibit strong agreement between the 13-week forecast and the verifying analysis (Fig. 13b, c). The upward doming of the isotherms associated with the deep cyclone, more pronounced in the deep ocean, is reasonably well predicted in the 13-week forecast. A similar feature is also observed in the 7-week forecast (valid on January 27) initialized from the December 9 analysis (Fig. 9e, f). The analysis on October 28, which shows nearly flat isotherms below 1000 m, does not support the presence of a deep cyclone, indicating that its development is not constrained during the initial conditions (Fig. 13a). The strong eastward current around 25°N characterizes the location of the LC, with isotherms gradually shoaling to the north. The consistent presence of the deep cyclone in these forecasts enhances our confidence in the extended predictability of LCE separation.

3.5. LCE transformation

3.5.1. Predictability of LCE transformation following separation

We now focus on the LCE transformation after its separation on January 27. In the four weeks following the separation on January 27, the LCE undergoes minimal modifications, as depicted in the analysis in Fig. 3i-l. We examine the predictability of the LCE on February 24, 2020. Fig. 14 illustrates the characteristics of the LCE on February 24, 2020, as predicted by the prior 7-week forecasts. The forecasts demonstrate good agreement among the drifter and SSHA observations, analysis, and forecasts across all lead times up to 7 weeks. The ensemble system accurately predicts the location and size of the LCE. There are cyclones

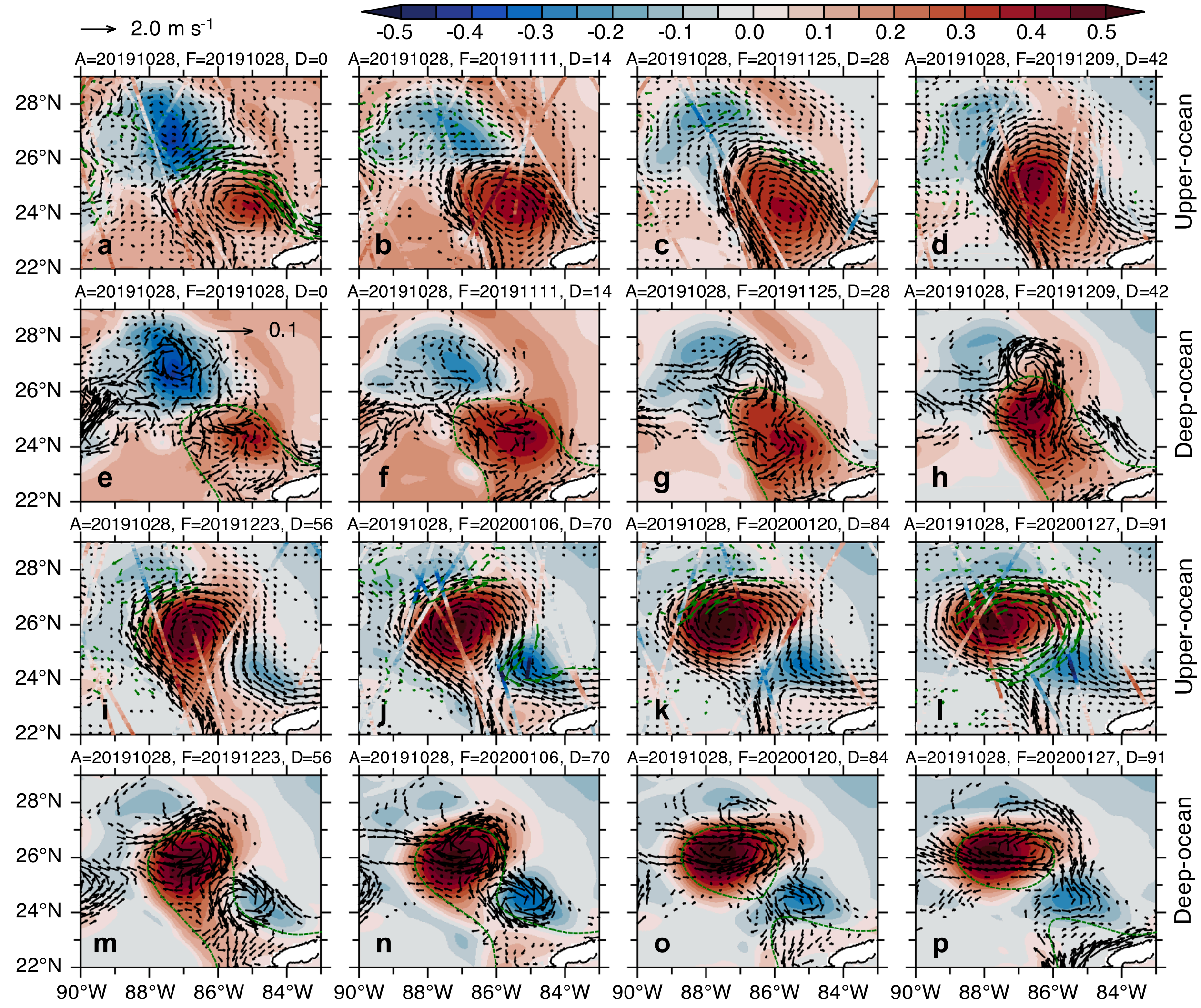

Fig. 12. Bi-weekly ensemble mean surface currents and deep currents (averaged over 1000–2000 m) (m s^{-1}), and Sea Surface Height Anomaly (SSHA, m) from a 13-week forecast initialized from the October 28, 2019 analysis. (Note: forecasts for weeks 12 and 13 are weekly rather than bi-weekly.) Surface current panels are overlaid with drifter velocity observations (green vectors) and along-track SSHA altimetry observations during the 7–day and 5–day periods preceding each forecast lead time, respectively. Drifter observations are binned onto a 0.4° × 0.4° grid. Deep current panels include the 0.17 m Sea Surface Height (SSH, m) contour. Vectors are displayed for surface (deep) currents exceeding 0.1 (0.02) m s^{-1}.

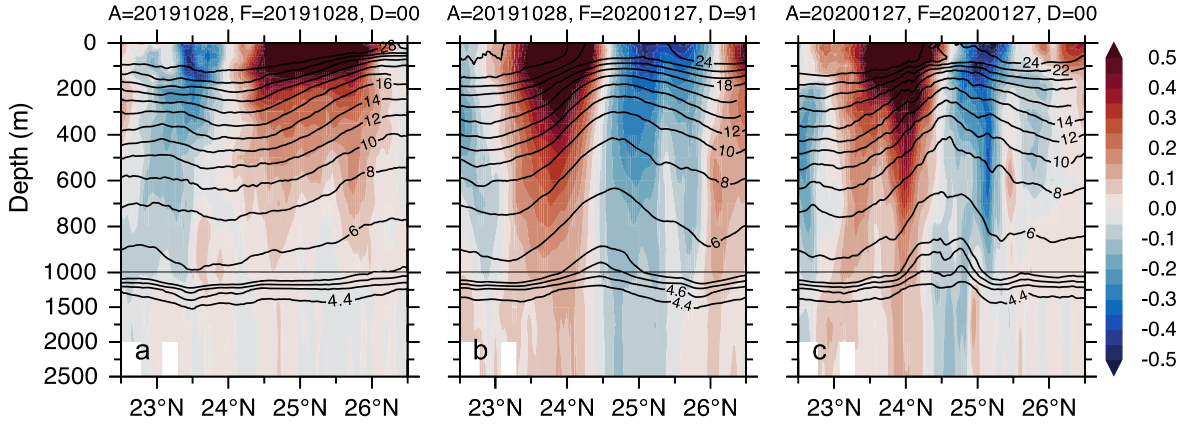

Fig. 13. Vertical sections of temperature (contours, °C) and zonal velocity (shaded, m s^{-1}) from (a) analysis on October 28, 2019 (b) 13-week forecast initialized on October 28, 2019 and valid on January 27, and (c) the verifying analysis on January 27, 2020. The fields are averaged over the region 84.5°–85.5°W. Positive (negative) velocity indicates eastward (westward) flow. The westward current around 25°N indicates the northern flank of the cyclone. Contour intervals are 0.05 m s^{-1} for velocity and 2 °C for temperature (note that contour intervals differ below 1000 m). The 13-week forecast uses ensemble member 25 to better capture the core of the current associated with the cyclone, while the 32-member ensemble mean reveals a similar pattern but with, weaker intensity.

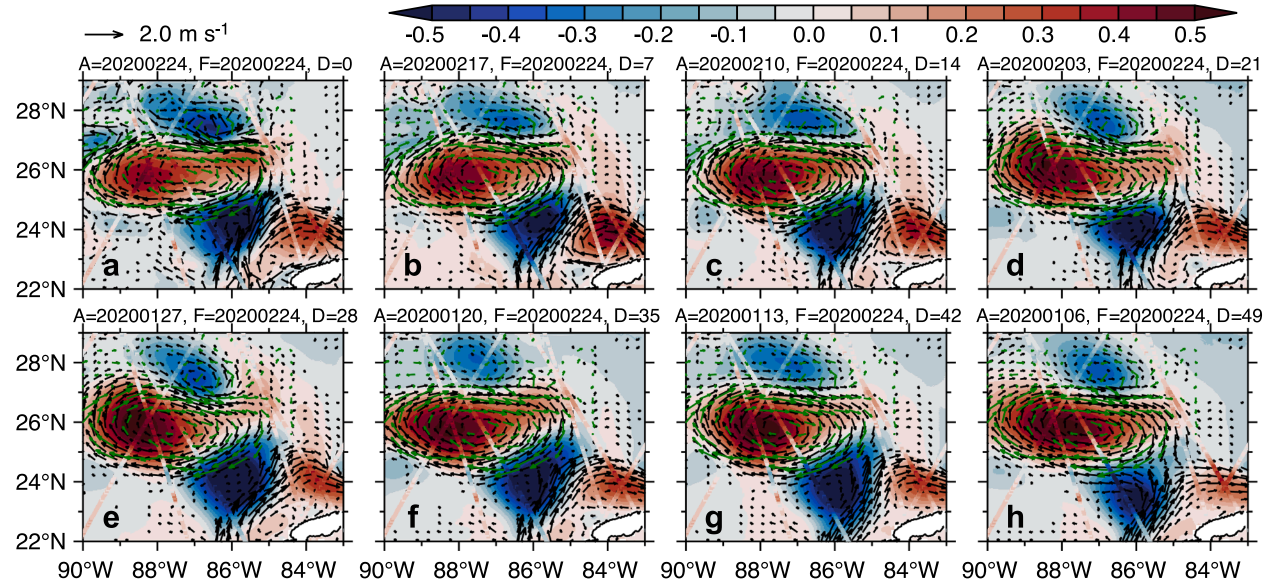

Fig. 14. Ensemble mean surface currents (m s^{-1}) and Sea Surface Height Anomaly (SSHA, m) from forecasts initialized up to 7 weeks prior and valid on February 24, 2020. Surface current panels are overlaid with drifter velocity observations (green vectors) and along-track SSHA altimetry observations during the 7–day and 5–day periods preceding the valid time, respectively. Drifter observations are binned onto a 0.4° × 0.4° grid. The first panel represents the verifying analysis, which serve as the reference against which all prior forecasts are compared. Vectors are displayed for currents exceeding 0.1 m s^{-1}.

on either side of the LCE, causing the LCE to expand zonally to ~ 550 km (from 90°W to 85°W). The cyclone to the north of the LCE at 87°W, 27°N, which is also confirmed in the drifter observations, is weaker than the one to the south. All forecasts predicted the existence of these cyclones, although their exact locations differ slightly among forecasts at different lead times. The aforementioned southern cyclone between the LC and LCE is located farther south in forecasts with longer lead times compared to the analysis (Fig. 14a). In the 7-week forecast, the cyclone is positioned at 86°W, 23.5°N, whereas in the analysis, it is located at 86°W, 24°N, a difference of ~ 60 km. Similarly, the cyclone north of the LCE in the 7-week forecast (Fig. 14h) is slightly northwest compared to the analysis (Fig. 14a), although its exact location can only be confirmed by the positions of two drifters. The forecasts also represent a realistic retracted LC at all lead times, consistent with the analysis.

The location of the cyclones in the analyses (Fig. 3e-k), which served as initial conditions for these forecasts, are different. For example, in the January 6 analysis (Fig. 3e), the cyclone along the northern edge of the LCE is located around 88°W, 27.5°N. However, during the 7-week forecast initialized from January 6 analysis, the cyclone gradually propagated eastward to 87°W, 27.5°N (Fig. 14h). Similarly, the cyclone to the south of the LCE drifted southwestward across the LC to 86°W, 23.5°N from its initial location (85°W, 24.5°N) in the analysis. The fact that these cyclones were constrained during the analyses and served as the initial conditions for the forecasts contributes to the predictive skill

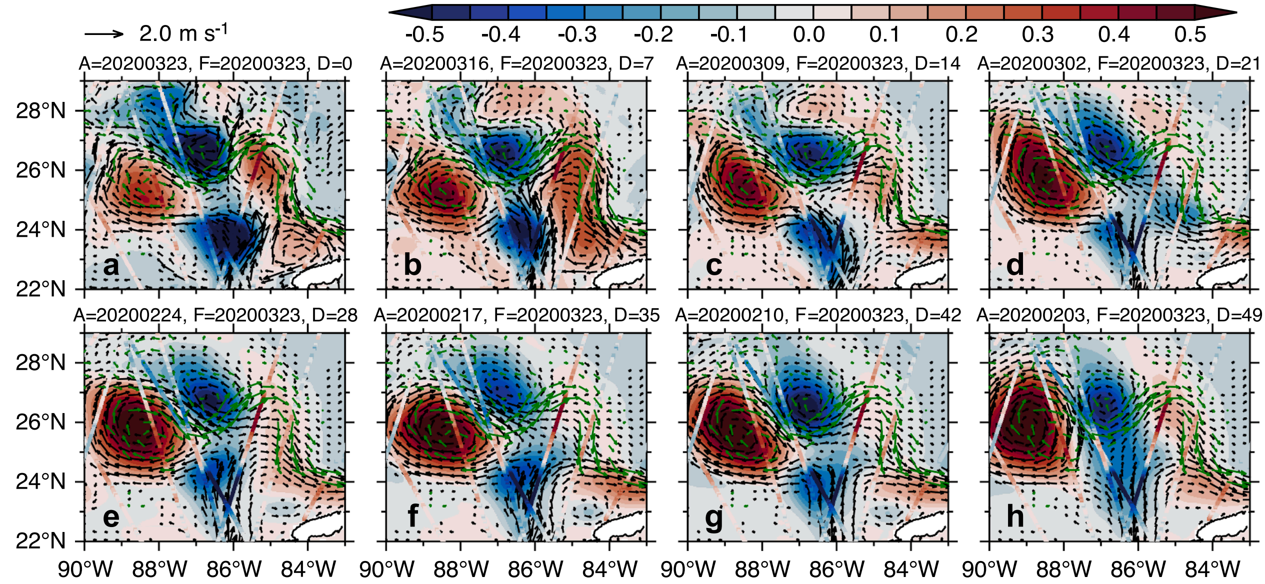

Fig. 15. Ensemble mean surface currents (m s^{-1}) and Sea Surface Height Anomaly (SSHA, m) from forecasts initialized up to 7 weeks prior and valid on March 23, 2020. Surface current panels are overlaid with drifter velocity observations (green vectors) and along-track SSHA altimetry observations during the 7–day and 5–day periods preceding the valid time, respectively. Drifter observations are binned onto a 0.4° × 0.4° grid. The first panel represents the verifying analysis, which serve as the reference against which all prior forecasts are compared. Vectors are displayed for currents exceeding 0.1 m s^{-1}.

of the model. The structure and location of the LCE are influenced by the interaction between the LCE and these cyclones.

Between February 24 and March 23, notable transformations occur in the LCE, transitioning from a zonally elongated LCE on February 24 (∼550 km) to two distinct and nearly separated anticyclones by March 23 (Fig. 3l-p). The predictability of this transformation in the ensemble system is explored by examining the March 23, 2020 forecasts. The prior 7-week forecasts valid on March 23, depicted in Fig. 15, demonstrate the ensemble model's ability to simulate the interaction between the LCE and cyclones that lead to the LCE transformation. The analysis (Fig. 15a) identifies two nearly separated LCEs located at 88°W, 25°N and 85°W, 26°N respectively, which aligns with the independently verification from drifter observations. These LCEs are separated by a large cyclone along the northern edge of the LCE, extending about 150 km in the zonal direction (86°–87.5°W). The center of this cyclone (87°W, 26.5°N), as indicated by SSHA, compares well with the drifter observations. Furthermore, this cyclone is partially connected to an adjacent cyclone located northwest at 88°W, 28°N, although northwestern cyclone is significantly weaker than its southeastern counterpart. The northwestern cyclone at 88°W, 28°N does not remain distinct from the other cyclone after the 1–2 week forecast. The forecasts also capture this pair of cyclones, although they appear as a single large cyclone at longer lead times.

In the forecasts shown in Fig. 15, there are notable differences in the characteristics of the LCE compared to the analysis. The western part of the LCE tends to be larger and stronger in the forecasts, while the eastern counterpart is weaker and smaller, as indicated by the SSHA. The western part consistently appears in all forecasts, although there are variations in its location, size, and intensity compared to the analysis. This is confirmed by the drifter observations, which show the center of the LCE in the 7-week forecast located at 89°W, 26°N (Fig. 15h), farther northwest of its location in the analysis (Fig. 15a). The eastern lobe of the LCE exhibits mixed predictability in the forecasts, particularly in terms of its strength. While the surface currents in the forecast align with the track of the drifter observations, the forecasts tend to underestimate the magnitude of the lobe, especially at the 3-week lead time. These discrepancies between the forecasts and observations can be ascribed to the presence of cyclones and their interactions with the LC and the LCE. The forecasts adequately represent the presence of cyclones, but their characteristics differ among the forecasts at different lead times. For example, the 7-week forecast initialized from February 3 (Fig. 15h) accurately places the cyclone along the northern edge of the LCE at 87°W, 26.5°N, while the one in the south is poorly represented. During the analysis on March 23, the southern cyclone is located around 86°W,

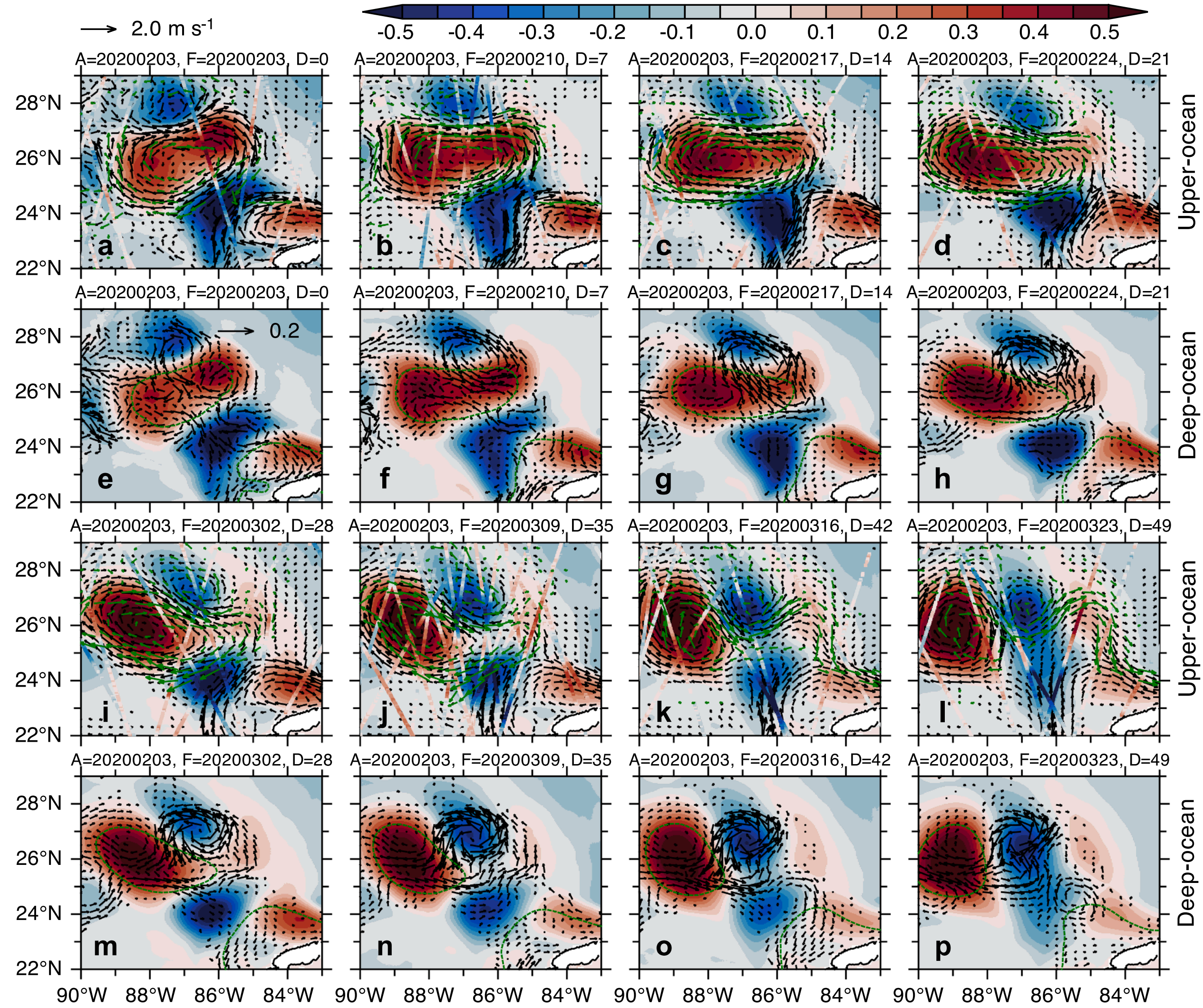

Fig. 16. Ensemble mean surface currents and deep currents (averaged over 1000–2000 m) (m s^{-1}), and Sea Surface Height Anomaly (SSHA, m) from a 7-week forecast initialized from the February 3, 2020 analysis. Surface current panels are overlaid with drifter velocity observations (green vectors) and along-track SSHA altimetry observations during the 7–day and 4–day periods preceding each forecast lead time, respectively. Drifter observations are binned onto a 0.4° × 0.4° grid. Deep current panels include the 0.17 m Sea Surface Height (SSH, m) contour. Vectors are displayed for surface (deep) currents exceeding 0.1 (0.02) m s^{-1}.

23.5°N (Fig. 15a). While this cyclone consistently appears in all forecasts, there are differences in its location, size, and intensity, particularly at longer lead times. The forecasts tend to underestimate the intensity of the cyclone compared to the observations of along-track SSHA, which show stronger negative SSHA in the cyclonic region. The location of the cyclone influences the bifurcation of the LC, with a majority of flow directing eastward to form a retracted LC. This mismatch, particularly in the intensity of the cyclone, between the observations and forecasts contributes to the differences in the simulation of the LC and the eastern part of the LCE. Despite these shortcomings in the structure of the LCE, the forecasts still capture the realism of the LCE transformation associated with the cyclones.

3.5.2. *Evolution of upper and deep ocean circulation*

The single 7 weeks forecast initialized from February 3, 2020 provides further insights into the interaction between the LCE and cyclones, particularly focusing on the deep circulation (Fig. 16). The analysis on February 3 (Fig. 16a) reveals a detached LCE from the LC, a retracted LC, and a cyclone (87.5°W, 28°N) along the northern edge of the LCE. These features are well constrained during the data assimilation, as supported by along-track SSHA observations and independent drifter verification. As the forecast progresses, it becomes evident that the cyclone along the northern edge of the LCE plays a crucial role in the transformation of the LCE. By week 3 of the forecast (Fig. 16d), this northern cyclone leads to weakening and narrowing of the eastern half of the LCE. The southeastward intrusion of this northern cyclone in the subsequent forecasts leads to the splitting of the LCE into two.

The deep circulation is dominated by a distinct cyclone, which is larger and exhibits different characteristics compared to the surface cyclone. The deep cyclone, which offset and lead the surface cyclone, bounded by the region 87.5°-85°W and 25°-28°N, extends southeastward into the entire LCE during the week 1–2 forecasts (Fig. 16f, g). At this stage, the surface cyclone is centered at 87°W, 27.5°N, while the deep cyclone is slightly to the southeast at 86.5°W, 27°N. As the deep cyclone progressively expands into the LCE, the LCE undergoes significant deformation. The deep cyclone transverses the eastern part of the LCE, resulting in partial spitting by week 4 and complete separation by week 7. In the early forecast lead times, the deep cyclone leads the surface cyclone. However, by the 6 weeks forecast (Fig. 16o), both the deep currents and surface SSHA indicate a vertical alignment of the cyclones. This alignment is primarily facilitated by the southeastward propagation of the surface cyclone, while the deep cyclone remains nearly stationary.

The comparison of the deep circulation in the forecast with the verifying analysis (Fig. 8e-h) shows good agreement. For instance, the location of the deep cyclone along the northern side of the LCE in the 3, 5, and 7-week forecasts (Fig. 16h, n, p), qualitatively agrees with that in the analysis (Fig. 8f, g, h). Although the deep ocean is largely unconstrained during the data assimilation, as the synthetic profiles derived from along-track SSHA only extend to the upper 1000 m (synthetic profiles below 1000 m are fitted with climatology), the forecast accurately captures the size, location, and the evolution of the cyclone along the northern edge of the LCE. The southward expansion of the cyclone into the LCE region and the vertical alignment of surface and deep cyclones in the forecasts align well with the analysis. Overall, the model forecasts demonstrate good skill in simulating the evolution and transformation of the LCE out to 7 weeks. The interaction between the LCE and deep and surface cyclone is found to be instrumental in the partitioning of the LCE.

The vertical sections of zonal velocity and temperature from the 6-

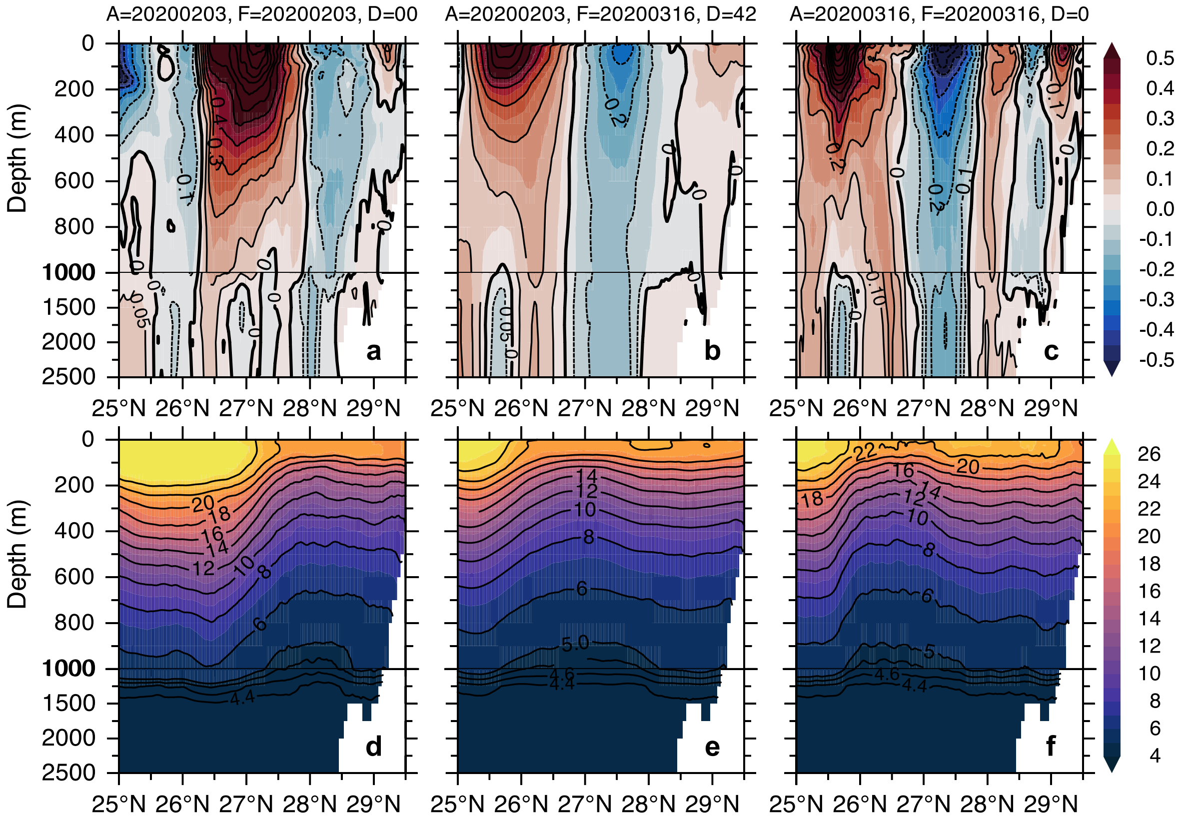

Fig. 17. Vertical sections of (a-c) zonal velocity (m s^{-1}) and (d-f) temperature (°C), comparing (a, d) the analysis on February 3, 2020; (b, e) the 6-week forecast initialized on February 3 and valid on March 16, 2020; and (c, f) the verifying analysis on March 16, 2020. All fields are averaged over the region 86.5°–87.5°W from the ensemble member 5. Positive (negative) velocity indicates eastward (westward) flow. The contour interval is 0.1 m s^{-1} for zonal velocity and 2 °C for temperature, with different contour intervals below 1000 m.

week forecasts, initialized from the analysis on February 3, and the verifying analysis provide (Fig. 17) further insights into the upper and deep parts of the cyclone in the north. The analysis on February 3 (Fig. 17a) reveals that the LCE is confined to south of 27.7°N, characterized by eastward flow on its northern side, and westward flow on its southern side. Surface velocities within the LCE exceed 1 m s^{-1} at 27°N, and gradually weaken to around 0.2 m s^{-1} at ~ 750 m. Conversely, the westward flow associated with the cyclone exhibits a surface intensified core exceeding 0.15 m s^{-1} between 28° and 29°N. The surface cyclone, predominantly situated north of 27.7°N, slightly offsets the deep cyclone, which is positioned farther south around 28°N. Velocities within the deep cyclone reach 0.10 m s^{-1} below 1000 m. The temperature sections indicate shoaling of isotherms at the location of the deep cyclone, particularly pronounced at deeper isotherms. The 5 °C isotherm experiences a vertical displacement of 100 m. Based on the crossing of the 5°C isotherm at 1000 m, the location of the deep cyclone can be identified between 27.3° and 28.7°N.

The analysis (Fig. 17c) and the 6-week forecast (Fig. 17b), valid on March 16, 2020, reveal a distinct flow pattern that corresponds to the weakening of the LCE. The northern flank of the LCE undergoes weakening in the vertical (0.2 m s^{-1} confined to 400 m) and shifts further south, with its core located around 26°N. Simultaneously, the upper and deep cyclones become more vertically aligned and have shifted southward, with the deep cyclone centered around 27.5°N and velocities of 0.15 m s^{-1}. While the locations of the major circulation features in the 6-week forecast are consistent with the analysis, their magnitudes are underestimated, particularly in the upper 300 m. For instance, the flow associated with the surface cyclone (27°–28°N, 0–300 m) and LCE (25°–26.5°N, 0–300 m) in the forecast is weaker by 35 % and 16 %, respectively, compared to the analysis. The temperature forecast shows a similar shoaling of the isotherms, although the difference is more pronounced at deeper isotherms where the analysis exhibits a sharper vertical displacement. Specifically, the 5 °C isotherm undergoes a shoaling of 100 m associated with the deep cyclone. It should be noted that the specific locations of these features may vary among different ensemble members, with some members potentially reproducing the flow pattern with greater accuracy than others, and the mean being a smoother version than any single member. Nevertheless, the forecast still demonstrates reasonable predictability and aids in the interpretation of the LCE transformation.

3.5.3. Deep cyclone validation

The independent deep current meter observations at two nearby locations B04 (86.78°W, 26.77°N) and C06 (85.59°W, 26.23°N) that measured current magnitude and direction at 50 m from the seafloor, provide validation for the presence of a deep cyclone in the model forecast (Johnson et al., 2022). The time-series of velocity vectors on either side of the cyclone during February – March 2020, displayed in Fig. 18, exhibit opposing deep currents, which are characteristics of a deep cyclone. Note that current meters were located approximately at the western and eastern boundaries of the deep cyclone (Fig. 8e-h). The current meter located on the eastern flank of the cyclone indicates a predominantly northward flow between February 10 and March 15, 2020. This was recorded near the bottom of the Gulf of Mexico at 3316 m. After March 15, the flow weakens as the deep cyclone shrinks or drifts away from the location of the current meter, which is consistent with the week 6–7 forecasts (Fig. 16o-p). The current speed gradually increased to a maximum value of 25 cm s^{-1} during late February to early March, followed by a gradual decline to 5 cm s^{-1}. The timing, intensification, and direction of the flow in the observations align with both the forecast (blue vectors) and the analysis (red vectors). However, the flow magnitude in the model is significantly underestimated. The time averaged observed current speed was 20 cm s^{-1}, while the model indicates a value of 10 cm s^{-1}.

At the northwest location B04, (133 km away from C06), the observed flow was predominantly south, indicating the western flank of the deep cyclone (Fig. 18a). However, it gradually became more southwest from late February to mid-March 2020. It is important to note that B04 was located at a slightly shallower depth of 3096 m compared to C06. In both the analysis (Fig. 18a) and forecast (Fig. 18b), the flow is south and southeasterly during the period when flow is northward at C06. It should be kept in mind that the flow structure is sensitive to the location of the deep cyclone and its orientation relative to the current meter. In the model, the flow becomes north to northeasterly in late March as the deep cyclone propagates westward, marking the eastern edge of the cyclone (Fig. 16o-p). The mismatch between the model and observation can be alluded to differences in the exact location and propagation of the deep cyclone. Additionally, it is worth noting that the shape of the deep cyclone in the model changes from a northwest/southeast in the week 2 to north/south elongated ellipse in the week 6 forecast (Fig. 16). The observations show a progressive increase in speed

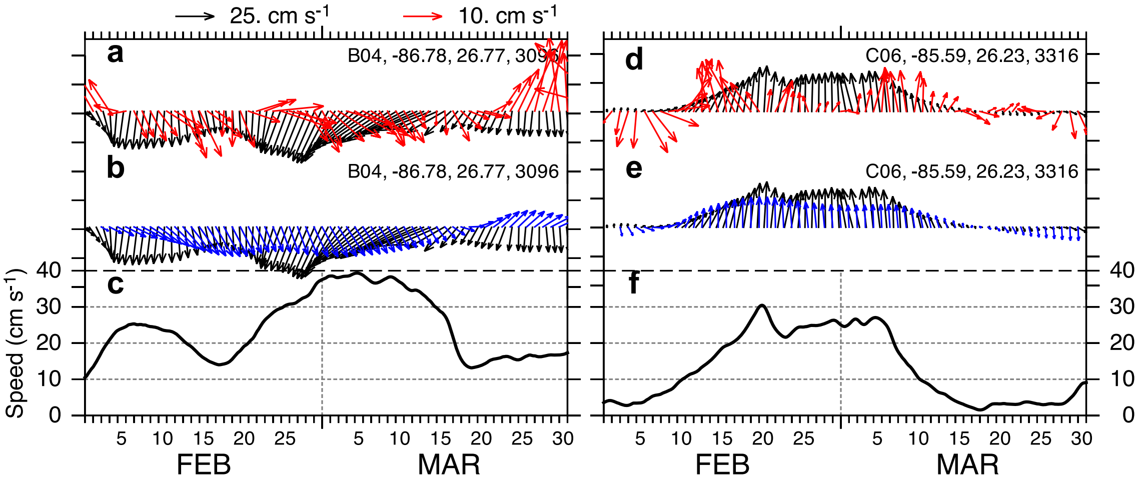

Fig. 18. Time-series of vector velocity (cm s^{-1}) from (a) model analysis (red) overlaid on current meter observations (black) (b) forecast initialized from February 3, 2020 analysis (blue) overlaid on current meter observations (black), and (c) observed speed, at a location B04 (86.78°W, 26.77°N, 3096 m depth). Panels (d–f) same as (a–c) but at a location C06 (85.59°W, 26.23°N, 3316 m depth). Note that the ensemble means currents are at 1500 m depth, with a reference vector of 10 cm s^{-1}, while the observations have a reference vector of 25 cm s^{-1}. The current meter was located near the western (B04) and eastern (C06) edges of the deep cyclone, as indicated by the green triangles in Fig. 8e-h. The February – March 2020 period covers the presence of the deep cyclone along the northern edge of the LCE. Hourly velocity observations are smoothed using a 49-hour Parzen filter.

from 15 cm s^{-1} in mid-February to a peak value of 38 cm s^{-1} in early March, followed by a decline to 15 cm s^{-1} after mid-March. However, the model flow is significantly weaker, half the magnitude of the observations, despite that fact that the model current is shallower (1500 m) compared to the observed depth (> 3000 m). Also note that the ensemble mean current is generally expected to be weaker. Nevertheless, the flow associated with the deep cyclone in both the analysis and forecasts qualitatively align with the observations. The model forecasts consistently demonstrate weakened currents, a characteristic that aligns with the earlier studies reporting an underestimation of Eddy Kinetic Energy (EKE) in the LC region, with values reaching only half of those observed (Rosburg et al. 2016; Morey et al., 2020).

3.6. Comparison with other LCE separation events

While the specific case study of Thor demonstrates the realism of the model forecast in capturing the sequence of events leading to LCE separation and subsequent deformation, it does not provide a comprehensive assessment of the overall predictability of LC/LCE shedding events. Forecast skill has been found to vary significantly across different LCE separation events since 2013, indicating that multiple factors contribute to LCE formation. These include both upper-ocean and deep-ocean circulation features, particularly the development of deep cyclones, and their interactions with the evolving LC and LCE. Such lateral and vertical interactions underscore the importance of upper-deep ocean coupling processes in shaping the LCE evolution. To further investigate this variability in forecast performance, we examine an additional LCE separation event, Ursa, which shares dynamic similarities with Thor but differs in its predictability. Unlike Thor, Ursa underwent two distinct detachment events: an initial brief separation on March 8, 2021, followed by reattachment, and a final separation on April 26, 2021, a sequence that has been more difficult for the model to predict compared to a single separation event. We focus here on both separation episodes to highlight the differences in their dynamical evolution and associated forecast skill.

The 7-week forecasts valid on March 8, 2021, and initialized from different analyses, show reasonable skill in capturing the timing and location of the initial Ursa separation (Fig. 19). Despite predicting near-complete LCE separation at all lead times, the forecasted structure of the LC and LCE differs from the verifying analysis (Fig. 19a). As in the Thor case, cyclonic eddies appear to the north and south of the LCE, but with notable differences: the northern cyclone is weaker, and the southern cyclone remains confined to the eastern flank of the LC, resulting in a partial attachment of the LC and LCE along the western boundary

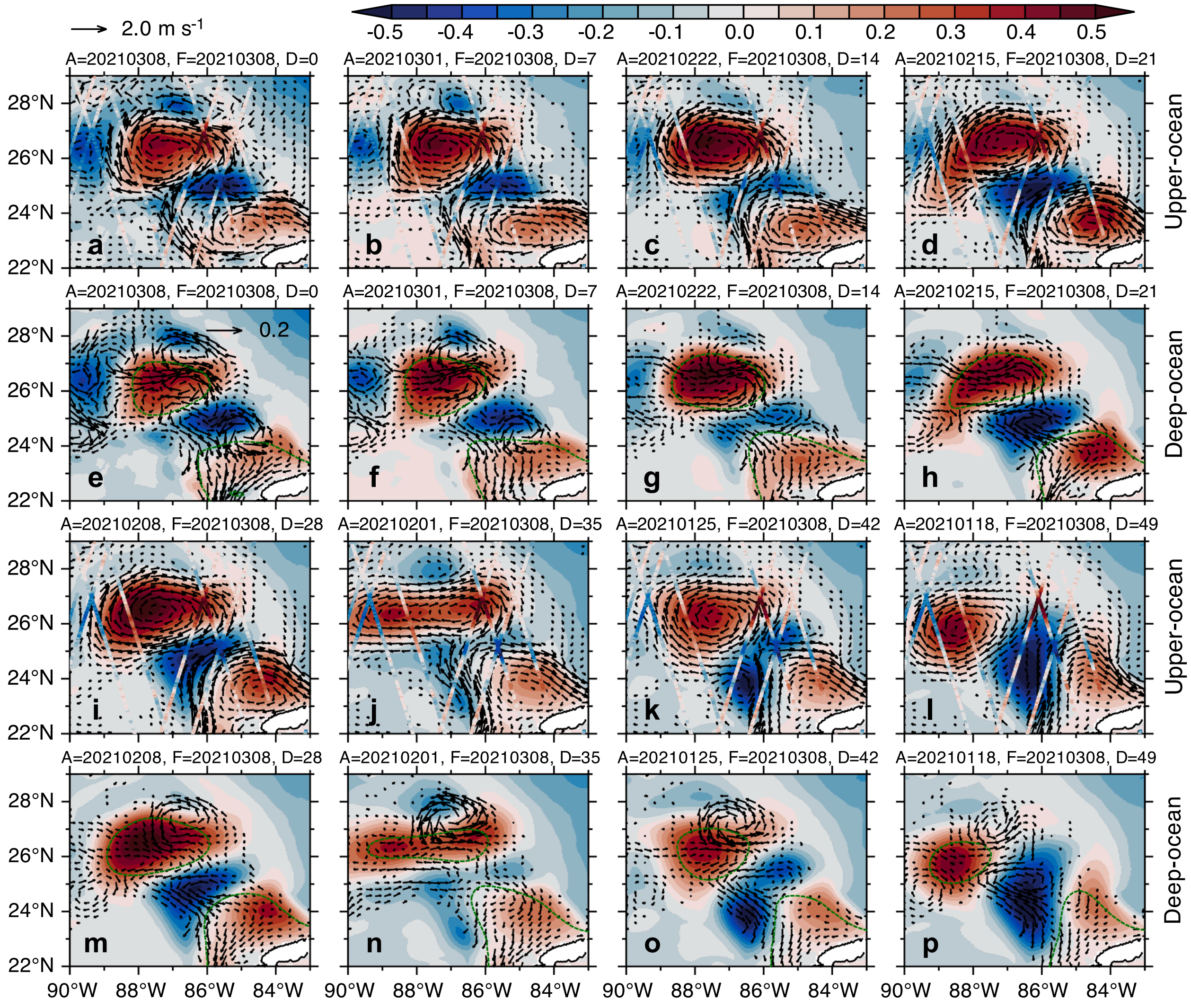

Fig. 19. Initial separation of Loop Current Eddy, Ursa. Ensemble mean surface currents, deep currents (averaged over 1000–2000 m) (m s^{-1}), and Sea Surface Height Anomaly (SSHA, m) are shown from forecasts initialized up to 7 weeks prior and valid on March 8, 2021. Surface current panels are overlaid with along-track SSHA altimetry observations from March 5–8, while deep current panels include the 0.17 m Sea Surface Height (SSH, m) contour. The first panel represents the verifying analysis, used as the reference truth against which all prior forecasts can be compared. Vectors are displayed for surface (deep) currents exceeding 0.1 (0.02) m s^{-1}.

(Fig. 19a). In the 3-, 4-, and 7-week forecasts, westward-extending cyclones across the LC promote premature or complete LCE detachment, while other lead times show only partial separation. The limited forecast skill in this case is attributed to the absence of a strong, persistent deep cyclone – a feature shown to be critical in the Thor event. Dissipation or weakening of this cyclone likely enabled near-reattachment as seen in the 5-week forecast. A secondary cyclone near the western boundary (90°–89°W, 26°N), evident in the 1–3 week surface forecasts, also plays a role in modulating the LCE structure. While the northern deep cyclone is present across all forecasts, its intensity varies, it is weaker in the 3-week and stronger in the 5-week forecast. A combination of a stronger northern cyclone and the absence of a western boundary cyclone in the 5-week forecast appears to promote the development of a more zonally elongated LCE (Fig. 19j). These results emphasize the operational need to resolve the structure, intensity, and evolution of deep cyclones and their interaction with the LC to improve the accuracy and lead time of LCE separation forecasts.

The 7-week forecast initialized from the analysis on March 8, 2021, captures the sequence of detachment, reattachment, and eventual separation (Fig. 20). The model reasonably simulates the brief detachment during March 8–15, followed by reattachment approximately one week later (March 22), and final separation on April 26. The cyclone along the eastern flank of the LC, which initially contributed to the March 8 detachment, weakens progressively with lead time, resulting in a reattachment. By the 3-week forecast (Fig. 20d), this cyclone has significantly weakened, and by week 5, it dissipates further, with remnants evident near 84°W, 24°N (Fig. 20j-n). As the southern cyclone weakens and shifts southward, the northern deep cyclone begins to propagate southward, manifesting at the surface as an increasingly undulating LC. By week 3 (Fig. 20h), it is located near 86°W, 26°N, just north of the dissipating southern cyclone (85°W, 25°N), and is accompanied by a deep anticyclone to the north (87°W, 28°N). The alignment of eastern flank of the LC with the northern deep cyclone combined with topography may have facilitated its southward propagation. The arrival of this northern cyclone initiates the ‘necking down’ of the LC (Fig. 20i), eventually leading to the LCE separation by week 7, as indicated by the altimeter SSHA low and the 0.17 m SSH contour. Despite this, the LC and LCE remain partially attached along the western boundary at the surface. From weeks 5–7, the deep cyclone remains its strength and position, playing a key role in Ursa’s final detachment. A deep anticyclone is also present in the 4–6 week forecasts, eventually weakening as a northern deep cyclone emerges in week 6–7.

Although the timing of Ursa’s separation is reasonably well captured in the 7-week forecast, the structure of the LCE differs from both the

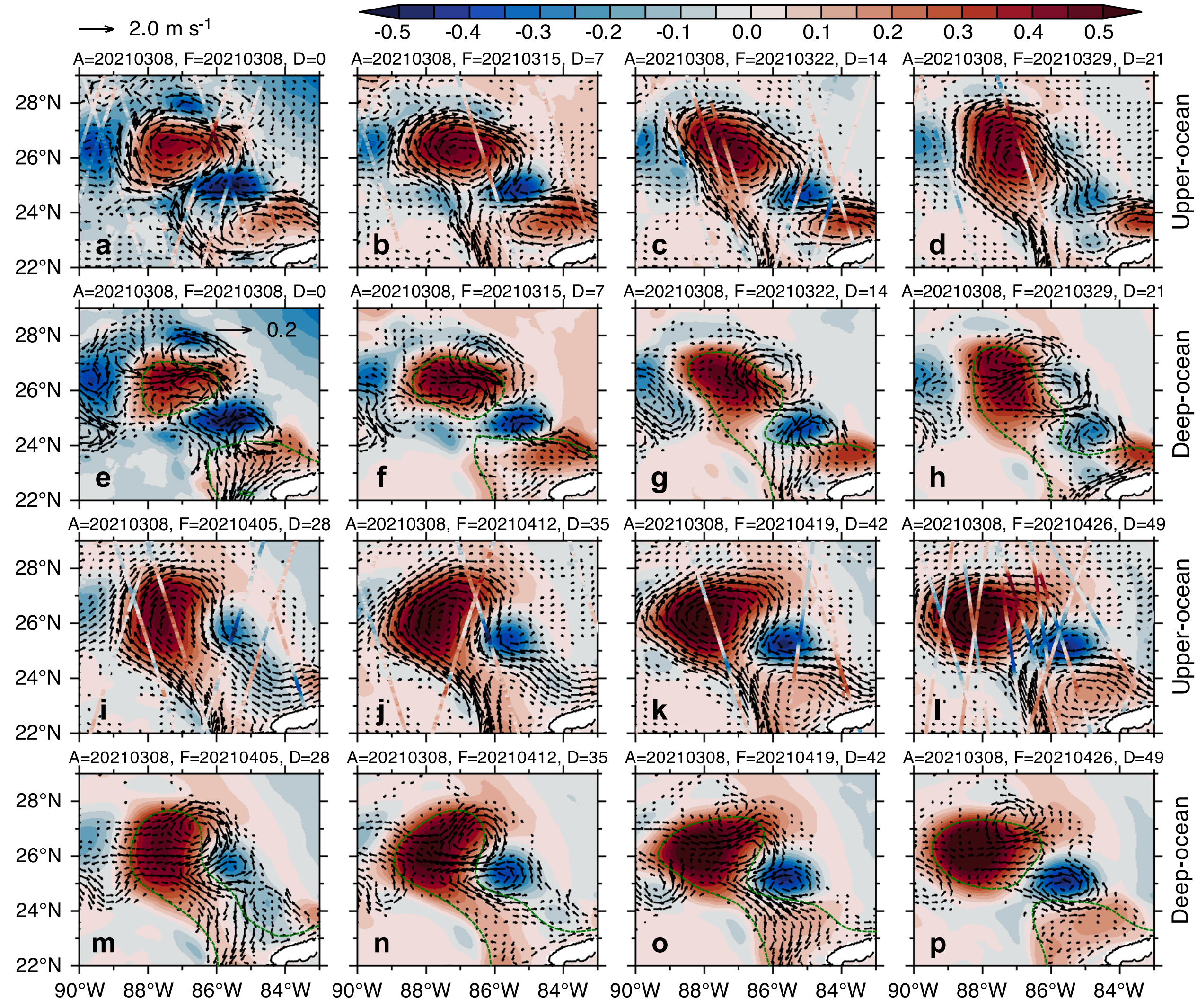
A=20210308, F=20210308, D=0
A=20210308, F=20210315, D=7
A=20210308, F=20210322, D=14
A=20210308, F=20210329, D=21
A=20210308, F=20210308, D=0
A=20210308, F=20210315, D=7
A=20210308, F=20210322, D=14
A=20210308, F=20210329, D=21
A=20210308, F=20210405, D=28
A=20210308, F=20210412, D=35
A=20210308, F=20210419, D=42
A=20210308, F=20210426, D=49
A=20210308, F=20210405, D=28
A=20210308, F=20210412, D=35
A=20210308, F=20210419, D=42
A=20210308, F=20210426, D=49

Fig. 20. Final separation of Loop Current Eddy, Ursa. Ensemble mean surface currents and deep currents (averaged over 1000–2000 m) (m s^{-1}), and Sea Surface Height Anomaly (SSHA, m) from a 7-week forecast initialized from the March 8, 2021 analysis. Surface current panels are overlaid with along-track SSHA altimetry observations during the 4–day period preceding each forecast lead time. Deep current panels include the 0.17 m Sea Surface Height (SSH, m) contour. Vectors are displayed for surface (deep) currents exceeding 0.1 (0.02) m s^{-1}.

verifying analysis (not shown) and altimeter observations (Fig. 20l). Both depict a more zonally elongated LCE (oriented northeast-southwest) than that represented in the forecast. In the April 26 analysis, the LCE aligns with a deep anticyclone and is accompanied by a weak deep cyclone along its northern boundary (not shown), resembling, for example, the deep circulation in the 6-week forecast (Fig. 20o), except with the southern deep cyclone in the analysis extending farther west. While the southern deep cyclone plays a central role in both Thor and Ursa separations, in the case of Ursa, it appears to originate from a preceding northern deep cyclone that propagated southward. These comparisons further underscore the complex upper-deep ocean interactions that influence LCE structure and timing.

4. Discussion and conclusions

A 32-member ensemble forecast system for the Gulf of Mexico is employed to investigate the predictability of the Loop Current (LC) and Loop Current Eddy (LCE), particularly focusing on the LC/LCE separation of the LCE Thor that occurred in January 2020. The evaluation of the model forecast using various observations and verifying analyses demonstrates that the model realistically represents the evolution of the LC, its northward extension into the Gulf of Mexico, and the separation of the LCE from the LC during the December 2019 to March 2020 time period. The timing of LC/LCE separation in the forecast aligns closely with the observations, demonstrating its capability to predict this event. Specifically, in the studied event, the model accurately predicted the LCE separation 13 weeks in advance.

Analysis of a characteristic LCE shedding event highlights the significance of the interaction between the LC and a deep cyclone along the eastern edge of the LC. While previous studies have reported on the role of such interactions in LC/LCE detachment, this study adds a new dimension by demonstrating the model's ability to predict the eddy shedding event up to 13 weeks in advance. This extended prediction capability enabled a detailed analysis of the underlying processes involved in LCE shedding, offering further insights into the evolution of the deep cyclone. The findings are supported by an independent evaluation using concurrent deep current meter observations, which confirmed the presence of the deep cyclone reaching the near bottom (> 3000 m) of the Gulf of Mexico. The intensification and westward expansion of the deep cyclone played a crucial role in the eventual separation of the LCE from the LC on January 27, 2020. While previous studies have suggested the involvement of one or more cyclones during the necking down phase (Schmitz, 2005; Le Henaff et al., 2012), this study provides evidence of a single deep cyclone interacting with the LC during the detachment period. Furthermore, the deep cyclone leads the surface cyclone by approximately a week, suggesting that the surface cyclone develops through coupling between the upper and deep ocean via baroclinic instability (Hogan and Hurlburt, 2000; Hurlburt and Thompson, 1980; Zhu and Liang, 2020).

After separation, the LCE undergoes rapid transformations primarily due to interactions with a cyclone located along its northern edge. This cyclone consistently appears in that region prior to the LCE separation. Initially, a deep cyclone offsets and leads the surface cyclone, gradually aligning vertically and undergoing intensification. As a result of the expansion and intrusion of the deep cyclone under the LCE, the eddy nearly splits into two, with the eastern portion partially joining the LC. This cyclone along the northern edge of the LCE, similar to the deep cyclone along the eastern edge of LC, extends down to the near bottom of the Gulf of Mexico. Independent current meter observations confirm the existence of this deep cyclone, with current speeds exceeding 35 cm s^{-1} at a depth of 3096 m. The timing and characteristics of the deep and surface cyclones in the forecast align with the observations, although the model underestimates the magnitude of the deep currents by more than 50 %.

While the case studies presented here demonstrate the model's capability in capturing the critical role of deep cyclones in LCE separation and its predictability, the detailed mechanisms underlying the formation of these deep cyclones remain unexplored. Nonetheless, we provide a brief overview of the existing hypotheses that may explain the generation of deep cyclones associated with LCE separation. The coupling between the upper and deep ocean around the meandering Loop Current (LC) has been proposed as a key mechanism for the formation of deep cyclones, primarily through layer stretching to conserve potential vorticity (Hamilton et al., 2011). When the LC develops a trough, the associated increase in lower-layer thickness generates a deep cyclone that typically leads the upper-layer trough. Hamilton et al. (2011) identified three such LC trough–deep cyclone pairs—along the eastern, northern, and western edges of the LC—during the formation of LCE Franklin between May 12–20, 2010. These features closely resemble those observed during the brief LCE Ursa event (Fig. 19a), and the presence of deep cyclones to the north and south in the Thor case suggests similar LCE evolution pathways. As the LC intrudes into shallower regions, such as the Mississippi Fan and the northeastern Gulf of Mexico, the formation of a deep cyclone–anticyclone pair in the lower layer has been documented both observationally (Hamilton et al., 2011) and in modeling studies (Welsh and Inoue, 2000). The development of a deep cyclone to the north of the LC, which offsets the surface SSHA low, is consistent with a baroclinic instability arising from the meandering upper-layer jet. The "necking down" of the LC along its eastern flank—often a precursor to LCE separation—is thought to result from the amplification of meandering troughs through upper–deep eddy interactions (Donohue et al., 2016). Modeling work by Le Hénaff et al. (2012) further suggests that when upper-layer frontal cyclones propagate over the Mississippi Fan, they can induce the formation of a deep cyclone. This upper–deep cyclone pair then propagates across the LC and facilitates LCE detachment. The final separation of LCE Ursa on April 26, 2021, is consistent with the influence of a southward-propagating deep cyclone—likely guided by topographic features, from the Mississippi Fan to the Campeche Bank, ultimately triggering the separation.

In their energy budget analysis, Yang et al. (2020) suggest that deep eddies derive their energy primarily from the upper layer through vertical pressure work, and secondarily from baroclinic instability in the deep layer. More recently, Yang et al. (2023) show that both buoyancy forcing and barotropic instability also play important role in the generation of cyclonic eddies. Deep eddies may further gain energy through upper-ocean topographic coupling through transfer of EK via baroclinic instability (Hogan and Hurlburt, 2000; Thoppil et al., 2011). The surface and abyssal ocean circulations are strongly coupled through energy cascades that vertically redistribute the energy and vorticity throughout the entire water column. At the surface, kinetic energy is dominated by EKE, which arises from mean flow instabilities and direct wind forcing. Through nonlinear eddy-eddy interactions, energy cascades from large scales down to the Rossby radius scale and vorticity towards small scales. Near the Rossby radius scale, energy is transferred downward into the deep ocean, facilitating vertical coupling. In the abyss, eddies interact with underlying topography, giving rise to persistent mean flows and further modulating the deep circulation (Thoppil et al., 2011).

We find a relationship between the vorticity at the Yucatan Channel and the downstream development of a deep cyclone, although a detailed investigation of the underlying dynamical processes is not conducted in this study. The relative vorticity (s^{-1}) averaged between 1000–2000 m in the Yucatan Channel (21°–22°N) during a 13-week forecast initialized from the October 28, 2019 analysis is shown in Fig. 21. The results indicate the presence of high values of cyclonic (positive) vorticity from early December 2019 to late January 2020. These periods of strong cyclonic vorticity, with values exceeding 4×10^{-6} s^{-1}, precede the formation of the deep cyclone. This is consistent with the appearance of a deep cyclone on December 9 (Fig. 12h). The persistence of cyclonic vorticity until late January likely contributes to the maintenance of the deep cyclone, separation of the LCE, and the retraction of LC. The vorticity peaks in early December with a secondary peak in January,

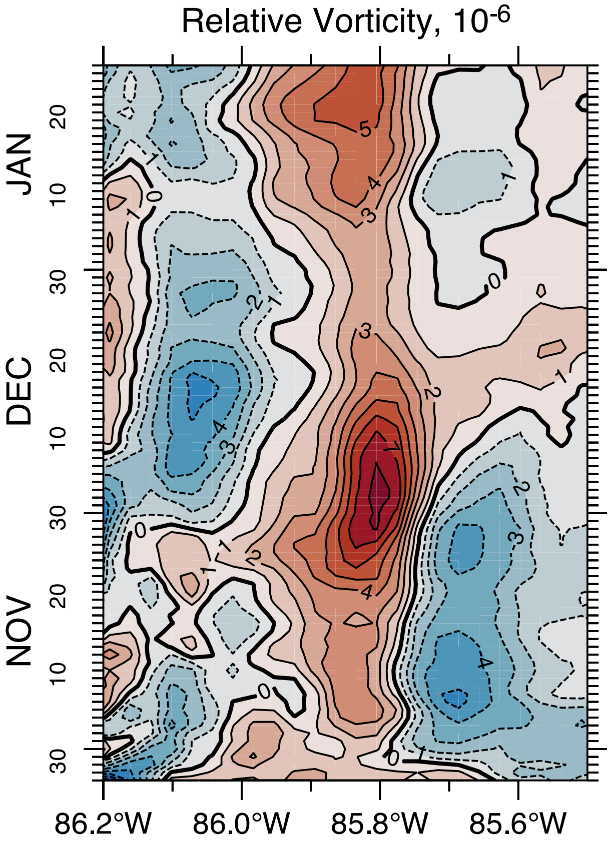

Fig. 21. Temporal evolution of relative vorticity (10^{-6}, s^{-1}) averaged over 1000–2000 m along the Yucatan Channel between 21°–22°N from the 13-week (91-day) forecast initialized from the analysis on October 28, 2019. The development of a deep cyclone during December coincides with the higher values of cyclonic vorticity.

coinciding with the separation of the LCE. The vorticity fluxes resulting from horizontal shear through the Yucatan Channel have previously been identified as influential factor in the behavior of the LC in the Gulf of Mexico (Candela et al., 2002; Oey, 2004). Similarly, Androulidakis et al. (2014) attribute the generation and growth of cyclone to regions of high positive vorticity in the Campeche Bank. While the exact mechanism remains uncertain, it is reasonable to assume that both the position and intensity of the Yucatan inflow play a critical role in initiating and shaping the deep cyclone. Further analysis and dedicated model experiments are needed to disentangle the relative contributions of the inflow dynamics, topographic steering, and baroclinic processes.

The results of this study highlight the potential to further improve forecast skill by reducing uncertainties of the model initial conditions. One effective approach is to increase the density of the ocean observations network. In particular, deep ocean circulation remains largely unconstrained in a data assimilative systems due to the limited availability of subsurface observations. Sparse deep Argo observations are insufficient for effectively constraining deep mesoscale features. While the assimilation of altimeter observations can inject energy into the upper ocean and enhance the representation of deep EKE by transferring energy downward via baroclinic instability (Thoppil et al. 2011), its impact on deep ocean circulation is limited to approximately 1000 m, the maximum depth of synthetic profiles. Consequently, error growth in the forecast is expected to be higher in the deep ocean compared to the upper ocean, which may partly explain the varying predictability in LCE formation. Furthermore, the model forecasts consistently demonstrate weaker subsurface currents, which aligns with the findings of earlier studies reporting an underestimation of EKE under the LC region by one-half of when compared to observations (Rosburg et al., 2016; Morey et al., 2020). Enhancing the predictability of LC/LCE shedding events in the Gulf of Mexico requires strengthening the deep ocean observing network and integrating these observations into data assimilation systems. In particular, the routine use of targeted, feature-based adaptive sampling in regions of cyclones formation could help constrain bottom circulation and improve forecast skill. Ongoing efforts, such as the Understanding Gulf Ocean Systems (UGOS) program, are actively working to assimilate deep ocean observations and leverage new platforms like the Surface Water and Ocean Topography (SWOT) mission to improve the prediction of Gulf of Mexico ocean dynamics.

CRediT authorship contribution statement

Prasad G. Thoppil: Writing – review & editing, Writing – original draft, Visualization, Validation, Supervision, Software, Project administration, Methodology, Investigation, Funding acquisition, Formal analysis, Data curation, Conceptualization. **Clark D. Rowley:** Writing – review & editing, Writing – original draft, Validation, Software, Resources, Data curation. **Patrick J. Hogan:** Writing – review & editing, Writing – original draft, Validation, Methodology. **James Stear:** Writing – review & editing, Writing – original draft, Validation, Methodology.

Declaration of competing interest

The authors declare the following financial interests/personal relationships which may be considered as potential competing interests: Prasad Thoppil reports financial support was provided by Chevron Research and Technology. If there are other authors, they declare that they have no known competing financial interests or personal relationships that could have appeared to influence the work reported in this paper.

Acknowledgments

This work was supported by the CASE EJIP funding from the Chevron Research and Technology. The computational resources were provided by the Naval Research Laboratory, Stennis Space Center, Mississippi, USA. Drifter observations from the Woods Hole Group (WHG) is greatly appreciated. This NRL contribution NRL/JA-7320-25-6814. It has been approved for public release and distribution is unlimited. SST observations were provided by JPL under support by NASA MEaSUREs program. We thank the reviewers for their valuable comments, which greatly improved the manuscript.

Data availability

Bottom current meter data analyzed in the study can be found in the GRIIDC data depository and https://data.gulfresearchinitiative.org/data/U1. x852.000:0003 and DOI:10.7266K4ZF1T9Z. The along-track altimeter observations are publicly available from AVISO. The drifter observations are obtained from Woods Hole Group (WHG) as part of the ensemble forecast system development. Interested parties may contact WHG directly. The model output is the product of NRL and sponsors, and release of output can only be permitted through collaboration or approval upon reasonable request to corresponding author.

References

Androulidakis, Y.S., Kourafalou, V.H., Le Hénaff, M., 2014. Influence of frontal cyclone evolution on the 2009 (Ekman) and 2010 (Franklin) Loop current eddy detachment events. Ocean Sci. 10, 947–965.

Barth, A., Alvera-Azcárate, A., Weisberg, R.H., 2008. Assimilation of high-frequency radar currents in a nested model of the West Florida Shelf. J. Geophys. Res. 113 (C8).

Barton, N., et al., 2020. The Navy's Earth system prediction capability: a new global coupled atmosphere-ocean-sea ice prediction system designed for daily to subseasonal forecasting. Earth Space Sci. 8, e2020EA001199.

Bishop, C., Toth, E.T., 1999. Ensemble Transformation and adaptive observations. J. Atmos. Sci. 56 (11), 1748–1765.

Candela, J., Sheinbaum, J., Ochoa, J., Badan, A., Leben, R., 2002. The potential vorticity flux through the Yucatan Channel and the loop current in the Gulf of Mexico. Geophys. Res. Lett. 29 (22), 161–164.

Carrier, M.J., Ngodock, H.E., Muscarella, P., Smith, S., 2016. Impact of assimilating surface velocity observations on the model sea surface height using the NCOM-4DVAR. Mon. Weather Rev. 144, 1051–1068.

Chassignet, E., Hurlburt, H., Smedstad, O., Halliwell, G., Hogan, P., Wallcraft, A., Baraille, R., Bleck, R., 2007. The HYCOM (HYbrid Coordinate Ocean Model) data assimilative system. J. Mar. Syst. 65 (1–4), 60–83.

Cochrane, J.D., 1972. Separation of an anticyclone and subsequent developments in Loop Current. Contributions on the Physical Oceanography of the Gulf of Mexico, 2. Gulf Publishing Co, pp. 91–106.

Coelho, E.F., Peggion, G., Rowley, C., Jacobs, G., Allard, R., Rodriguez, E., 2008. A note on NCOM temperature error calibration using the ensemble transform. J. Mar. Syst., Rapid Environmental Assessment Special Issue 78, S272–S281.

Counillon, F., Bertino, L., 2009. High-resolution ensemble forecasting for the Gulf of Mexico eddies and fronts. Ocean Dyn. 59 (1), 83–95.

Cummings, J.A., 2005. Operational multivariate ocean data assimilation. Q. J. R. Meteorol. Soc. 131, 3583–3604.

D'Addezio, J.M., Smith, S., Jacobs, G.A., Helber, R.W., Rowley, C., Souopui, I., Carrier, M.J., 2019. Quantifying wavelengths constrained by simulated SWOT observations in a submesoscale resolving ocean analysis/forecasting system. Ocean Model 135, 40–55.

Dobla-Reyes, F., Hagerdorn, R., Palmer, T.N., 2005. The rationale behind the success of multi-model ensembles in seasonal forecasting – II. Calibration and Combination. Tellus 57A, 234–252.

Donohue, K.A., Watts, D.R., Hamilton, P., Leben, R., Kennelly, M., 2016. Loop current eddy formation and baroclinic instability. Dyn. Atmos. Oceans 76 (2), 195–216.

Dukhovskoy, D.S., Leben, R.R., Chassignet, E.P., Hall, C.A., Morey, S.L., Nedbor-Gross, R., 2015. Characterization of the uncertainty of loop current metrics using a multidecadal numerical simulation and altimeter observations. Deep Sea Res. I 100, 140–158.

Fox, D., Teague, W., Barron, C., Carnes, M., Lee, C., 2002. The modular ocean data assimilation system (MODAS). J. Atmos. Oceanic Technol. 19 (2), 240–252.

Fratantoni, P.S., Lee, T.N., Podesta, G.P., Muller-Karger, F., 1998. The influence of Loop Current perturbations on the formation and evolution of Tortugas eddies in the southern Straits of Florida. J. Geophys. Res. 103 (C11), 24759–242779.

Furey, H., Bower, A., Perez-Brunius, P., Hamilton, P., Leben, R., 2018. Deep eddies in the Gulf of Mexico observed with floats. J. Phys. Oceanogr. 48 (11), 2703–2719.

Gopalakrishnan, G., Cornuelle, B.D., Hoteit, I., 2013a. Adjoint sensitivity studies of loop current and eddy shedding in the Gulf of Mexico. J. Geophys. Res. Oceans 118, 3315–3335.

Gopalakrishnan, G., Cornuelle, B.D., Hoteit, I., Rudnick, D.L., Owens, W.B., 2013b. State estimates and forecasts of the loop current in the Gulf of Mexico using the MITgcm and its adjoint. J. Geophys. Res. Oceans 118, 3292–3314.

Hamilton, P., Donohue, K.A., Leben, R.R., Lugo-Fernandez, A., Green, R.E. Loop Current observations during spring and summer of 2010: Description and historical perspectives, in Monitoring and Modeling the Deepwater Horizon Oil Spill: A record breaking enterprise (2011) *Geophys. Monogr. Ser.*, 195, pp. 117–130. Edited by Y. Liu et al., AGU, Washington, D. C., doi:10.1029/2011GM001116.

Helber et al., 2022. Velocity assimilation with improved synthetic ocean profiles (ISOP2): Validation Test Report, NRL/7320/MR—2022/6, Naval Research Laboratory.

Helber, R.W., Smith, S.R., Jacobs, G.A., Barron, C.N., Carrier, M.J., Rowley, C.D., Ngodock, H.E., Yaremchuk, M., Pasmans, I., Bartels, B.P., DeHaan, C.J., 2023. Ocean drifter velocity data assimilation, Part 1: Formulation and diagnostic results. Ocean Model 183, 102195.

Hodur, R.M., 1997. The naval research laboratory's coupled ocean atmosphere mesoscale prediction system (COAMPS). Mon. Weather Rev. 125, 1414–1430.

Hogan, P.J., Hurlburt, H.E., 2000. Impact of upper ocean – topographical coupling and isopycnals outcropping in Japan/East Sea models with 1/8° to 1/64° resolution. J. Phys. Oceanogr. 30, 2535–2561.

Hoteit, I., Hoar, T., Gopalakrishnan, G., Collins, N., Anderson, J., Cornuelle, B., Kohl, A., Heimbach, P., 2013. A MITgcm/DART ensemble analysis and prediction system with application to the Gulf of Mexico. Dyn. Atmos. Oceans 63, 1–23.

Huang, H.S., Walker, N.D., Hsueh, Y., Chao, Y., Leben, R.R., 2013. An analysis of loop current frontal eddies in a ⅛° Atlantic Ocean model simulation. J. Phys. Oceanogr. 43, 1924–1939.

Hurlburt, H., Thompson, J.D., 1980. A numerical study of loop current intrusions and eddy shedding. J. Phys. Oceanogr. 10 (10), 1611–1651.

Jacobs, G.A., et al., 2014. Data assimilation considerations for improved ocean predictability during the Gulf of Mexico Grand Lagrangian Deployment (GLAD). Ocean Model 83, 98–117.

Jacobs, G.A., D'Addezio, J.M., Bartels, B., Spence, P.L., 2021. Constrained scales in ocean forecasting. Adv. Space Res. 68, 746–761.

Johnson, A.R., Donohue, K.A., Watts, D.R., Tracey, K.L., Kennelly, M.A., 2022. Generation of high-frequency topographic Rossby waves in the Gulf of Mexico. Front. Mar. Sci. 9, 1049645.

Le Hénaff, M., Kourafalou, V.H., Morel, Y., Srinivasan, A., 2012. Simulating the dynamics and intensification of cyclonic Loop Current Frontal Eddies in the Gulf of Mexico. J. Geophys. Res. 117, C02034.

Leben, R.R., 2005. Altimeter-derived loop current metrics. In: Sturges, W., Lugo-Fernandez, A. (Eds.), *Circulation in the Gulf of Mexico: Observations and Models*. American Geophysical Union, pp. 181–201.

Lin, X.-H., Oey, L.-Y., Wang, D.-P., 2007. Altimetry and drifter data assimilations of loop current and eddies. J. Geophys. Res. 112, C05046.

Martin, P.J., Barron, C.N., Smedstad, L.F., Campbell, T.J., Wallcraft, A.J., Rhodes, R.C., Rowley, C., Townsend, T.L., Carroll, S.N., 2009. User's Manual for the Navy Coastal Ocean Model (NCOM) version 4.0 NRL Report NRL/MR/7320–09-9151.

Metzger, E.J., Smedstad, O.M., Thoppil, P.G., Hurlburt, H.E., Cummings, J.A., Wallcraft, A.J., Zamudio, L., Franklin, D.S., Posey, P.S., Phelps, M.W., Hogan, P.J., Bub, F.L., Dehaan, C.J., 2014. US navy operational global ocean and arctic ice prediction systems. Oceanography 27 (3), 32–43.

Morey, S.L., Gopalakrishnan, G., et al., 2020. Assessment of numerical simulations of deep circulation and variability in the Gulf of Mexico using recent observations. J. Phys. Oceanogr. 50, 1045–1064.

Oey, L.-Y., 2004. Vorticity flux through the Yucatan Channel and Loop current variability in the Gulf of Mexico. J. Geophys. Res. 109 (C10), C10004.

Oey, L., 2008. Loop current and deep eddies. J. Phys. Oceanogr. 38, 1426–1449.

Oey, L., Lee, H., 2002. Deep eddy energy and topographic Rossby waves in the Gulf of Mexico. J. Phys. Oceanogr. 32 (12), 3499–3527.

Oey, L.-Y., Lee, H.-C., Schmitz, W.J., 2003. Effects of winds and Caribbean eddies on the frequency of loop current eddy shedding: a numerical model study. J. Geophys. Res. 108 (C10), 3324.

Oey Jr., L.-Y., Ezer, T., Lee, H.-C., 2005. Loop Current, Rings and Related Circulation in the Gulf of Mexico: A Review of Numerical Models and Future Challenges. In: Sturges, W., Lugo-Fernandez, A. (Eds.), *Circulation in the Gulf of Mexico: Observations and Models*, pp. 31–56.

Palmer, T.N., 1988. Medium and extended range predictability and stability of the Pacific/North American mode. Q. J. R. Meteorol. Soc. 114, 691–713.

Palmer, T.N., 2019a. The ECMWF ensemble prediction system: looking back (more than) 25 years and projecting forward 25 years. Q. J. R. Meteorol. Soc. 145, 12–24.

Palmer, T.N., 2019b. Stochastic weather and climate models. Nat. Rev. Phys. 1, 463–471.

Pérez-Brunius, P., Furey, H., Bower, A., Hamilton, P., Candela, J., García-Carrillo, P., Leben, R., 2018. Dominant circulation patterns of the deep gulf of Mexico. J. Phys. Oceanogr. 48 (3), 511–529.

Rosburg, K.C., Donohue, K.A., Chassignet, E.P., 2016. Three-dimensional model-observation comparison in the loop current region. Dyn. Atmos. Oceans 76, 283–305.

Rudnick, D.L., Gopalakrishnan, G., Cornuelle, B., 2015. Cyclonic eddies in the Gulf of Mexico: Observations by underwater gliders and simulations by numerical model. J. Phys. Oceanogr. 45, 313–326.

Sandery, P.A., Sakov, P., 2017. Ocean forecasting of mesoscale features can deteriorate by increasing model resolution towards the submesoscale. Nat. Commun. 8, 1566.

Schmitz, W.J., 2005. Cyclones and westward propagation in the shedding of anticyclonic rings from the Loop Current. In: Sturges, W., Lugo-Fernández, A. (Eds.), Circulation in the Gulf of Mexico: Observations and Models. 161, American Geophysical Union, Washington, DC, pp. 241–261.

Smith, S.R., Helber, R.W., Jacobs, G.A., Barron, C.N., Carrier, M.J., Rowley, C.D., Ngodock, H.E., Pasmans, I., Bartels, B.P., DeHaan, C.J., Yaremchuk, M., 2023. Ocean drifter velocity data assimilation, Part 2: Forecast validation. Ocean Model 183, 102260.

Sturges, W., Lugo-Fernández, A., 2005. Circulation in the Gulf of Mexico: Observations and Models (Eds.). 161, American Geophysical Union. Geophysical Monograph Series, Washington, DC, 161, 360 pp.

Surcel, M., Zawadzki, I., Yau, M.K., 2014. On the filtering properties of ensemble averaging for storm-scale precipitation forecasts. Mon. Weather Rev. 142, 1093–1105.

Thoppil, P.G., Frolov, S., Rowley, C.D., et al., 2021. Ensemble forecasting greatly expands the prediction horizon for ocean mesoscale variability. Commun. Earth Environ. 2, 89.

Thoppil, P.G., Metzger, E.J., Hurlburt, H.E., Smedstad, O.M., Ichikawa, H., 2016. The current system east of the Ryukyu Islands as revealed by a global ocean reanalysis. Prog. Oceanogr. 41, 239–258.

Thoppil, P. G., Richman, J.G., Hogan, P.J., 2011. Energetics of a global ocean circulation model compared to observations. *Geophys. Res. Lett.*, L15607.

Vukovich, F.M., 1988. On the formation of elongated cold perturbations off the Dry Tortugas. J. Phys. Oceanogr. 18, 1051–1059.

Vukovich, F.M., Maul, G.A., 1985. Cyclonic eddies in the eastern Gulf of Mexico. J. Phys. Oceanogr. 15, 105–117.

Walker, N. D., Leben, R., Anderson, S., Feeney, J., Coholan, P., Sharma, N., 2009. Loop Current frontal eddies based on satellite remote sensing and drifter data. U.S. Dept. of the Interior, Minerals Management Service, Gulf of Mexico OCS Region, OCS Study MMS 2009-023, 78 pp.

Wei, M., Jacobs, G., Rowley, C., Barron, C.N., Hogan, P., Spence, P., Smedstad, O.M., Martin, P., Muscarella, P., Coelho, E., 2016. The performance of the US Navy's RELO ensemble, NCOM, HYCOM during the period of GLAD at-sea experiment in the Gulf of Mexico. Deep Sea Res. II 129, 374–393.

Wei, M., Rowley, C., Martin, P., Barron, C., Jacobs, G., 2013. The U.S. Navy's RELO ensemble prediction system and its performance in the Gulf of Mexico. Q. J. R. Meteorol. Soc. 139A.

Wei, M., Toth, Z., Wobus, R., Zhu, Y., Bishop, C., Wang, X., 2006. Ensemble Transform Kalman Filter-based ensemble perturbations in an operational global prediction system at NCEP. Tellus 58A, 28–44.

Welsh, S.E., Inoue, M., 2000. Loop current rings and deep circulation in the Gulf of Mexico. J. Geophys. Res. 105 (C7), 16951–16959.

Xu, F.H., Oey, L.Y., Miyazawa, Y., Hamilton, P., 2013. Hindcasts and forecasts of loop current and eddies in the Gulf of Mexico using local ensemble transform Kalman filter and optimum-interpolation assimilation schemes. Ocean Model 69, 22–38.

Yang, H., Yang, C., Liu, Y., Chen, Z., 2023. Energetics during eddy shedding in the Gulf of Mexico. Ocean Dyn. 73, 79–90.

Yang, Y., Weisberg, R.H., Liu, Y., Liang, X.S., 2020. Instabilities and multiscale interactions underlying the loop current eddy shedding in the Gulf of Mexico. J. Phys. Oceanogr. 50 (5), 1289–1317.

Yin, X.Q., Oey, L.Y., 2007. Bred-ensemble ocean forecast of loop current and rings. Ocean Model 17, 300–326.

Zavala-Hidalgo, J., Morey, S.L., O'Brien, J.J., 2003. Seasonal circulation on the western shelf of the Gulf of Mexico using a high-resolution numerical model. J. Geophys. Res. 108 (3389), C12.

Zhu, Y., Liang, X., 2020. Coupling of the surface and near-bottom currents in the Gulf of Mexico. J. Geophys. Res. Oceans 125, e2020JC016488.